

A STUDY ON THE SURFACE CHEMISTRY OF LEAD CHALCOGENIDES  
NANOCRYSTALS AND PATCHY COLLOIDAL PARTICLES

A Thesis

Presented to the Faculty of the Graduate School

of Cornell University

In Partial Fulfillment of the Requirements for the Degree of

Master of Science

by

Hilda Alejandrina Mera Sosa

May 2016

© 2016 Hilda Alejandrina Mera Sosa

## ABSTRACT

We present an implicit-solvent density functional theory study of lead selenide (PbSe) and lead sulfide (PbS) nanocrystal surfaces and investigate the effect of solvation on the adsorption of ligands and the surface energies of PbS and PbSe. We determine the binding energies of ligands in solvent medium on {100}, {110}, and {111} facets of PbS and PbSe using density-functional theory with a polarizable continuum model to describe the solvent. We find that polar solvents significantly reduce the surface energies of PbSe and PbS and the ligand binding energies, whereas nonpolar solvents have negligible effects on surface energies and ligand adsorption. The results explain how polar solvents can be used to remove ligands from nanocrystal facets and provide guidance how to selectively remove ligands from specific surfaces. We also present work on patchy colloidal particles and propose the confinement of nonspherical patchy particles for photonic crystals.

## BIOGRAPHICAL SKETCH

I grew up in Texas and Mexico. I pursued a higher education at Texas A&M University and decided to study chemical engineering in 2007.

I dedicate this work to my parents, Hilda M. Mera and Pedro F. Mera, who have supported me all these years, and my older brother, Fernando D. Mera who has inspired me all these years to pursue a higher education in science.

## ACKNOWLEDGMENTS

I would like to acknowledge the Colman Foundation and the Diversity Programs in Engineering for providing me support. I would like to acknowledge Dr. Tobias Hanrath and Dr. Abraham Stroock for their support and guidance in my graduate career. I also want to acknowledge financial support from the National Science Foundation (NSF) for providing support for research studies. Computational resources from University of Texas, Texas Advanced Computing Center (TACC), The University of Tennessee Knoxville, The National Institute for Computational Sciences (NICS), and The Extreme Science and Engineering Discovery Environment (XSEDE) are also acknowledged. Additionally, I want to acknowledge the staff at Cornell Nanoscale Science and Technology Facility for providing me support when I needed tools and materials for research. Other facilities that I would like to acknowledge are the Cornell Center for Materials Research and the Nanobiotechnology Center. Lastly, I am grateful to many engineering students who provided me support in many ways, especially the Graduate Society of Women Engineers. I want to acknowledge Rose Agger, Gloria Aguirre, Malika Grayson, and Ilse van Meerbeek who always gave me support and advice during graduate school.

## TABLE OF CONTENTS

<b>1 Nanocrystals</b>	<b>1</b>
1.1 Introduction .....	1
1.2 Significant Previous Work .....	4
1.2.1 Surface Energies .....	4
1.2.2 Surfactant Capping Agents and Oxidation .....	4
1.2.3 Nanocrystal Shape and Control .....	5
1.2.4 Solvent Effects for Oleic Acid Capped PbSe Nanocrystals .....	6
1.3 Computational Methods .....	7
1.3.1 Density Functional Theory .....	7
1.3.2 Ligand Binding Energies .....	8
1.3.3 Crystal Structure Coordinates .....	9
1.3.4 Convergence Tests .....	9
1.3.5 Stable Configurations .....	10
1.3.6 Solvation Surface Energies .....	11
1.4 Results .....	12
1.4.1 Binding Energies .....	12
1.4.2 Solvation Surface Energies .....	14
1.5 Research Plan .....	17
1.5.1 Monofunctional and Bifunctional Ligands .....	17
1.5.2 Analysis of Ligand Binding .....	17
1.5.3 Silver Doped PbSe Surfaces .....	18
1.5.4 Surface Oxidation on PbSe Nanocrystals .....	18
1.6 Conclusion .....	19
References .....	21
<b>2 Photonic Crystals</b>	<b>25</b>
2.1 Introduction .....	25
2.1.1 Patchy Particles .....	27
2.1.2 Janus particles .....	29
2.1.3 Confinement of Anisotropic Colloids .....	32
2.1.4 Stöber Method .....	34
2.2 Experimental Methods .....	35
2.2.1 Synthesis of fluorescent silica particles .....	35
2.2.2 Preparation of colloidal solutions & silicon substrates .....	36
2.2.3 Spin-coating .....	38
2.2.4 Thin film deposition .....	38
2.2.5 Lift-off Techniques .....	39
2.2.6 Gold etching .....	39
2.2.7 Thiol treatment .....	40
2.2.8 Characterization .....	40
2.2.9 Confinement .....	41
2.3 Results .....	43
2.3.1 Fluorescent Silica Monodisperse Particles .....	43

2.3.2	PMMA Dimers .....	44
2.3.3	Hollow Silica Peanut Particles .....	45
2.3.4	Spin-coating silica particles.....	45
2.3.5	Spin-coating nonspherical particles.....	47
2.3.6	Nonspherical Patchy Particles .....	49
2.3.7	Confinement Silica Patchy Particles .....	51
2.4	Research Plan .....	53
2.4.1	Confinement of Janus particles .....	53
2.4.2	Confinement of Nonspherical Janus Particles .....	54
2.4.3	Monte Carlo Simulations.....	54
2.5	Conclusion.....	55
	References .....	56
	<b>Appendix</b> .....	<b>58</b>

## LIST OF FIGURES

Figure 1.1: Schematic of PbX crystal structures. a) Rock-salt structure. b) PbX{100}. c) PbX{110}. d) PbX{111}. X=Se,S. Pb in gray; Se & S in yellow.....	2
Figure 1.2: Illustration of lead acetate on a) a nanocrystal surface in vacuum ( $\epsilon = 1$ ) and b) in solvent medium ( $\epsilon > 1$ ) .....	3
Figure 1.3: (adapted from 39) FTIR of a PbSe-OA thin film in DMF .....	6
Figure 1.4: PbAA <sub>2</sub> on {100} PbSe surfaces. a) $E_b = 0.24$ eV (vacuum). b) $E_b = 0.42$ eV (vacuum), $E_b = -0.12$ eV (in DMF medium). c) $E_b = 0.30$ eV (vacuum). Pb in gray blue; Se in yellow; O in red; C in cyan; H in white. ....	10
Figure 1.5: Illustration of PbX slabs. a) {100} PbX. PbSe: $6.205 \text{ \AA} \times 6.205 \text{ \AA}$ ; PbS: $5.993 \text{ \AA} \times 5.993 \text{ \AA}$ . b) {110} PbX. PbSe: $8.775 \text{ \AA} \times 6.205 \text{ \AA}$ ; PbS: $8.476 \text{ \AA} \times 5.993 \text{ \AA}$ . c) {111} PbX. PbSe: $8.775 \text{ \AA} \times 8.775 \text{ \AA}$ ; PbS: $8.476 \text{ \AA} \times 8.476 \text{ \AA}$ .....	11
Figure 1.6: Binding energy plotted against $\epsilon$ for a) PbCl <sub>2</sub> on {100} PbS, b) organic ligands on {100} PbSe, and c) DMF on PbSe surfaces, $\theta=90^\circ$ . d) Binding energy plotted against surface coverage for {100} PbSe surface, $\theta=90^\circ$ .....	12
Figure 1.7: DMF adsorbed on {100} PbSe surface in vacuum with an $E_b$ of a) 0.22 eV, $E_{b,DMF} = -0.16$ eV for O(DMF)-Pb(PbSe) [ $\theta = 180^\circ$ ] distance difference, $d = 2.93 \text{ \AA}$ , b) 0.37 eV, $E_{b,DMF} = 0.062$ eV for O(DMF)-Pb(PbSe) [ $\theta = 90^\circ$ ], $d = 2.81 \text{ \AA}$ , and c) 0.023 eV, $E_{b,DMF} = -0.21$ eV for N(DMF)-Pb(PbSe) [ $\theta = 180^\circ$ ], $d = 2.88 \text{ \AA}$ . Pb in gray blue; N in blue; C in cyan; H in white; O in red; Se in yellow. {100} PbS surface: a) $E_b = 0.21$ eV, $E_{b,DMF} = -0.17$ eV. b) $E_b = 0.32$ eV, $E_{b,DMF} = 0.033$ eV. c) $E_b = -0.022$ eV, $E_{b,DMF} = -0.40$ eV ( $d = 2.90 \text{ \AA}$ for cases a-c in PbS surface) .....	13
Figure 1.8: PbSe and PbS Solvation Surface Energies.....	14
Figure 1.9: Surface energy of (100), (110), and (111) PbS facets changing with relative permittivity .....	15
Figure 1.10: Surface energy of (100), (110), and (111) PbSe facets changing with relative permittivity. ....	15
Figure 2.1: Periodic refractive index in 1D, 2D, and 3D [1].....	26
Figure 2.2: Techniques for synthesis and microfabrication of patchy particles [2].....	27
Figure 2.3: (left) Schematic models of distorted Kagome lattice 3-6-3-6 and 3-12 <sup>2</sup> , respectively from building blocks with ‘K’ and ‘Y’ bonding geometry.[8] (right). Optical images of hexagonal lattice formed by X-type silica patchy particles. ....	29
Figure 2.4: (a) Schematic of patchy particle preparation from colloidal monolayer: [1] metal deposition up to hemisphere, particle stamping, repeat [1], etching preferential from equatorial plane. (b) Change in polar angle (associated with patch size) as a function of etch time. Asymmetric patches form at times greater than 100 s. (c-e). Scanning electron microscope images of patchy particles with X, Y, and Z-bonding geometries.[8].....	29
Figure 2.5: (left) Illustration and scanning electron microscope image of one-patch Janus particle. (right) Schematic models and optical images of Janus particles confined in a wedge cell.[11].....	30

Figure 2.6: Optical images of Janus particles in binary mixture confined in wedge-cell and models of the particle patterns in wedge cells.[11].....	31
Figure 2.7: Confocal microscopy images (z-slice, side views) for anisotropic colloids (not patchy) under confinement. (a) aligned in-plane, hexagonal monolayer ( $1\Delta$ ) (b) buckled state (1B) (c) bilayer square structure ( $2\Box$ ) (d) bilayer hexagonal type I ( $2\Delta_I$ ) (e) bilayer hexagonal type II ( $2\Delta_{II}$ ).[13].....	32
Figure 2.8: Monte Carlo simulations for phase behavior corresponding to experiment. Rhombic phase (d) not observed due to challenging in reaching highest density phase regions.[13].....	33
Figure 2.9: $H^*-\phi$ phase diagram of dimers.[13] .....	34
Figure 2.10: Illustration of wedge-cells containing glass slides and cover slips.[22] ..	42
Figure 2.11: Top view and side view of a wedge-cell.[13].....	42
Figure 2.12: Fluorescent (RITC) silica particles synthesized using Stöber method with an average diameter of 580 nm and a coefficient of variation of 4.8%. Image illustrating crystallization and hexagonal packing of silica ( $\text{SiO}_2$ ) particles.....	43
Figure 2.13: Higher magnification of monodisperse fluorescent (RITC) silica particles synthesized using Stöber method with an average diameter of 580 nm and a coefficient of variation of 4.8%.....	44
Figure 2.14: Poly(methyl methacrylate) [PMMA] dimers spin coated at 500 rpm for 60 s in ethanol. $[\text{PMMA}]_{\text{Si}<100>} = 0.02795 \text{ g/mL}$ .....	44
Figure 2.15: Poly(methyl methacrylate) [PMMA] dimers spin coated at 500 rpm for 60 s in ethanol. $[\text{PMMA}]_{\text{Si}<100>} = 0.02795 \text{ g/mL}$ .....	45
Figure 2.16: Photograph of a 3-in silicon wafer containing a monolayer of 400 nm fluorescent silica particles $[\text{SiO}_2]_{\text{Si}<100>} = 0.111 \text{ g/mL}$ .....	46
Figure 2.17: Photograph of a 3-in silicon wafer showing brilliant opalescence of a monolayer of 400 nm fluorescent silica particles.....	46
Figure 2.18: Surface coverage of PMMA dimers spin coated at 500 rpm for 60 s in ethanol .....	47
Figure 2.19: $\text{SiO}_2$ hollow peanut-shaped particles spin coated at 200 rpm and 300 rpm for 30 s in ethanol $[\text{H}]_{\text{Si}<100>} = 0.0365 \text{ g/mL}$ .....	47
Figure 2.20: SEM image of 400 nm fluorescent silica particles spin coated at 500 rpm and 550 rpm for 60 s on a 3-in silicon wafer.....	48
Figure 2.21: PMMA patchy particles with X-bonding geometry having 25 nm Au and 4 nm Ti coating and a gold etching time of 60 s .....	49
Figure 2.22: PMMA patchy particles with X-bonding geometry having 25 nm Au and 4 nm Ti coating and a gold etching time of 60 s and excess gold thin films.....	50
Figure 2.23: $\text{SiO}_2$ hollow peanut-shaped patchy particles (X-bonding) having 25 nm Au and 3 nm Ti coating and a gold etching time of 90 s.....	51
Figure 2.24: (a) Optical image of fluorescent 2 $\mu\text{m}$ silica patchy particles confined in a wedge cell. Image taken by Angela Stelson. (b) second optical image of fluorescent 2 $\mu\text{m}$ silica patchy particles confined in a wedge cell. Image taken by Angela Stelson. (c) 2 $\mu\text{m}$ $\text{SiO}_2$ microparticles (4% solids) spin-coated at 4000 rpm for 60 s in n-	

butanol. (d) 2 $\mu\text{m}$ $\text{SiO}_2$ patchy particles (X-bonding) with 25 nm Au : 2 nm Ti coating & etched for 100 s .....	52
Figure 2.25: (a) 2 $\mu\text{m}$ silica patchy particles (X-bonding) with 25 nm Au and 2 nm Ti coating and gold etched for 40 s (b) selected particles in (a) .....	53

## LIST OF TABLES

Table 1.1: Fitting parameters for calculating solvation surface energy of PbS and PbSe facets.....	16
Table 2.1: Concentrations of chemicals used in the synthesis of 600 nm silica particles .....	35
Table 2.2: TES and milli-Q water volume and molar information for silica synthesis	36
Table 2.3: Parameters and Conditions used to make colloidal suspensions.....	37
Table S1: PbSe and PbS Simulation Cell Dimensions .....	58
Table S2: Ligand and PbSe and PbS Simulation Cell Dimensions.....	58
Table S3: Ligand Simulation Cell Dimensions .....	58
Table S4: Permittivity of Polar Solvents at 20°C and Dipole Moments .....	59

# CHAPTER 1

## NANOCRYSTALS

### 1.1 Introduction

Colloidal semiconductor nanocrystal quantum dots (NQDs) are innovative nanomaterials that can be applied in photovoltaic solar cell devices due to their unique and tunable electronic and optical properties.<sup>1-7</sup> NQDs are of potential interest for solar energy applications because the fabrication of thin-film quantum dot solar cells is economically viable, and the band gap of semiconductor quantum dots can be adjusted to reach high-electrical conversion efficiencies by capturing more solar radiation.<sup>3</sup> The simplest photovoltaic solar cell consists of two semiconductor layers, a p-type junction and an n-type junction, which absorbs photons emitted from ultraviolet (UV) sunlight.<sup>8</sup> Solar cells can have a maximum theoretical efficiency of 33.7% according to the Shockley-Queisser limit for a p-n single junction cell.<sup>9</sup> Multi-junction photovoltaic cells currently have the highest efficiencies which exceed 40%, whereas quantum dot solar cells have so far only achieved an efficiency of 5%.<sup>3</sup>

Semiconductor quantum dots range in size from 2–10 nm, and their shape can be tuned by choice of synthesis condition and capping ligands.<sup>2,10-13</sup> A particular group of nanocrystals that are of interest in solar energy applications are lead chalcogenide (PbX; X=S,Se) nanocrystals due to their size-dependent tunable band gaps and strong quantum confinement, which allows the generation of many electron-hole pairs (excitons).<sup>3,12-15</sup> The energy required to excite electrons from weakly-bonded electrons in the valence band into the conduction band is known as the fundamental band gap.<sup>9</sup> On the other hand, the energy required for photons to be absorbed is known as the optical band gap.<sup>6,11,14</sup> The optical band gap and the fundamental band gap differ in

energies due to the exciton binding energy.<sup>6,11,14</sup> The fundamental gaps of bulk lead selenide (PbSe) and lead sulfide (PbS) are 0.28 eV<sup>11</sup> and 0.41 eV,<sup>16</sup> respectively at 298 K. The excitons in PbSe and PbS have a Bohr radii of 46 nm and 18 nm, respectively, with corresponding binding energies of 16.4 meV and 5.74 meV, respectively.<sup>11,16-20</sup> PbSe and PbS have a rock-salt crystal structure<sup>15</sup> (Fig. 1.1-a), where the stoichiometric ratio of Pb to S and Pb to Se is 1:1. The investigated facets are illustrated in Figure 1.1 b-d and are denoted by a set of Miller indices  $\{hkl\}$ .

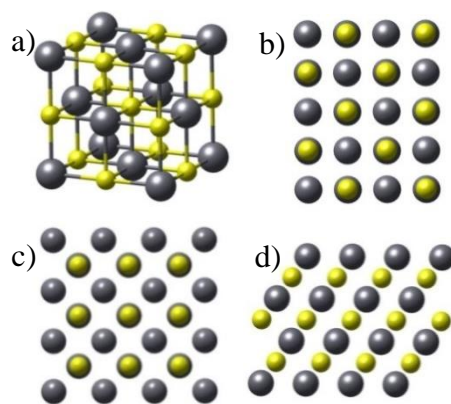


Figure 1.1: Schematic of PbX crystal structures. a) Rock-salt structure. b) PbX $\{100\}$ . c) PbX $\{110\}$ . d) PbX $\{111\}$ . X=Se,S. Pb in gray; Se & S in yellow.

Ligands prevent nanocrystal agglomeration, improve the conductivity of nanocrystal films, and stabilize colloidal nanocrystal quantum dots.<sup>1,21</sup> Figure 1.2-a illustrates ligand adsorption on nanocrystal surfaces, and Figure 1.2-b shows the desorption of ligands when a solvent is present in the system. The main purpose of the project is to account for solvent effects on ligand-capped lead chalcogenide nanocrystal surfaces in density-functional theory (DFT) calculations to determine ligand binding energies and also study doping effects in PbSe surfaces.<sup>22</sup> Density-functional theory solves the many-electron Schrödinger equation by replacing the problem of finding the many-

body wavefunction,  $\Psi$  with the much simpler problem of determining the ground-state electronic density,  $n(r)$ .<sup>23</sup> Using appropriate approximation choices for the exchange-correlation functional, DFT has been shown to provide accurate energies and electronic structures for many types of materials.<sup>23</sup> Moreover, molecular dynamics (MD) will be used to study the oxidation of lead chalcogenide surfaces.<sup>24</sup>

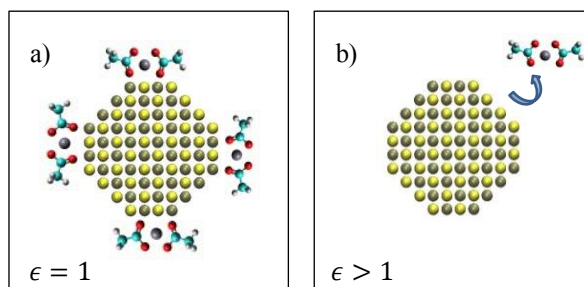


Figure 1.2: Illustration of lead acetate on a) a nanocrystal surface in vacuum ( $\epsilon = 1$ ) and b) in solvent medium ( $\epsilon > 1$ ).

In MD, Newton's equations of motion are integrated to find the thermodynamic properties of a system.<sup>25</sup> The implicit solvation model with linear polarization<sup>26</sup> will be used to describe the effect of solvents in ligand binding on lead chalcogenide surfaces by representing the solvent as a continuous medium surrounding the solute.<sup>27</sup> The implementation of a continuum solvent model in DFT calculations will reduce the number of degrees of freedom in a system and approximate long-range electrostatic forces in solvation phenomena<sup>27</sup> and provide new binding energies, electronic properties, and optical properties of ligands on lead chalcogenide surfaces. In this study, lead acetate<sup>2</sup> ( $\text{PbAA}_2$ ;  $\text{Pb}(\text{CH}_3\text{COO}^-)_2$ ), hydrazine<sup>21</sup> ( $\text{N}_2\text{H}_4$ ), dimethylformamide<sup>28</sup> (DMF;  $\text{C}_3\text{H}_7\text{NO}$ ), dithiolane<sup>29</sup> ( $\text{C}_3\text{H}_6\text{S}_2$ ), and lead chloride<sup>30</sup> ( $\text{PbCl}_2$ ) ligands are simulated on lead chalcogenide surfaces.

## **1.2 Significant Previous Work**

### **1.2.1 Surface Energies**

The surface energies of the {111}, {110}, and {100} PbSe facets in vacuum have been studied by Fang et al.<sup>31</sup> The {110} and {100} PbSe surfaces are stable, whereas the unreconstructed {111} PbSe surface is unstable. Fang et al.<sup>31</sup> created reconstructed and nonpolar {111} PbSe slabs where half of the surface lead atoms are removed from the Pb terminated surface and added atop the Se terminated surface of the slab. The surface energy of the {100} and {110} PbSe slabs were 11.4 meV/Å<sup>2</sup> and 19.84 meV/Å<sup>2</sup>, respectively.<sup>31</sup> The reconstructed {111} PbSe surface<sup>31</sup> had a surface energy of 20.5 meV/Å<sup>2</sup>. The linear polarization model<sup>26</sup> can be employed in DFT simulations to determine solvation surface energies of PbSe surfaces in DMF and study solvent effects on surface energies. The surface energies of PbSe surfaces in DMF will be compared to the {100}, {110}, and nonpolar {111} PbS surface energies in DMF.

### **1.2.2 Surfactant Capping Agents and Oxidation**

Dai<sup>32</sup> and collaborators studied the growth of PbSe nanocrystals in the presence of oleic acid surfactant agent and concluded that an increase in oleic acid resulted in a faster growth of PbSe nanocrystals.<sup>32</sup> Dai et al.<sup>32</sup> also observed a change in the PbSe nanocrystal shape when nanocrystals were exposed to air through Transmission Electron Microscopy (TEM) images. Dai et al.<sup>32</sup> recommended alkyl amine capping agents instead of oleic acid ligands because alkyl amines can prevent PbSe shrinking during storage.<sup>32</sup> Zarghami et al.<sup>33</sup> also observed the oxidation of PbS and PbSe QDs by noting a decrease in PbS and PbSe core diameters during air exposure using absorption spectra. Oxidation is therefore an important factor in PbSe and PbS

synthesis and storage.<sup>33</sup> MD simulations can be performed on ligand-capped PbSe NQDs in an oxygen (O<sub>2</sub>) or charged oxygen (O atoms) environment to study if the PbSe nanocrystal shape changes over time when capped with alkyl amines.<sup>24,34</sup>

### 1.2.3 Nanocrystal Shape and Control

Bealing et al.<sup>2</sup> demonstrated changes in the PbSe nanocrystal shape when PbSe was capped with different oleic acid ligands and acetic acid ligands. Bealing et al.<sup>2</sup> decided to study the oleic acid and acetic acid deprotonated anions on PbSe. Bealing et al.<sup>2</sup> assumed oleate and excess lead in the PbSe surface formed lead oleate ligands and predicted PbAA<sub>2</sub> formation when acetate reacted with excess lead. Based on the results obtained by Bealing et al.,<sup>2</sup> the nanocrystal shape transformed from a truncated octahedron to a cube as the lead oleate and PbAA<sub>2</sub> coverage increased. The binding energies of lead oleate on PbSe surfaces decreased nonlinearly as the surface coverage increased.<sup>2</sup> The work of Bealing et al.<sup>2</sup> neglected solvent interactions with ligands and PbSe surfaces. Choi et al.<sup>13</sup> performed DFT calculations of PbAA<sub>2</sub> adsorption on {100} and nonpolar {111} PbS surfaces and obtained higher PbAA<sub>2</sub> binding energies on the reconstructed {111} PbS surfaces. The linear polarization DFT model<sup>26</sup> can be used to study ligand-capped lead chalcogenide surfaces in hexane, chloroform, ethanol, and DMF, which are solvents used in PbSe and PbS synthesis,<sup>2,28,32-33,35</sup> and in propylene carbonate with a relative permittivity of 1.89, 4.806, 25, 36.71, and 64.9, respectively at 20°C.<sup>36</sup> Lastly, Bader charges<sup>37</sup> can be analyzed to validate PbAA<sub>2</sub> adsorption on PbSe and PbS surfaces.

### 1.2.4 Solvent Effects for Oleic Acid Capped PbSe Nanocrystals

In Rosen et al.<sup>28</sup> research work, oleic acid (OA) ligands were removed from PbSe surfaces in DMF medium. Dimethylformamide is a polar solvent with a relative permittivity of  $\epsilon = 36.71$  at 20°C.<sup>36,38</sup> Researchers in Hanrath Group in the Department of Chemical and Biomolecular Engineering at Cornell University also observed the removal of oleic acid from PbSe in DMF<sup>39</sup> by using Fourier transform infrared spectroscopy (FTIR) and concluded that DMF does not replace OA ligands when the PbSe-OA QD films are treated with DMF for short and long periods of time (1-60 min) because DMF IR peaks were not observed in PbSe-OA absorption spectra (see Figure 1.3).

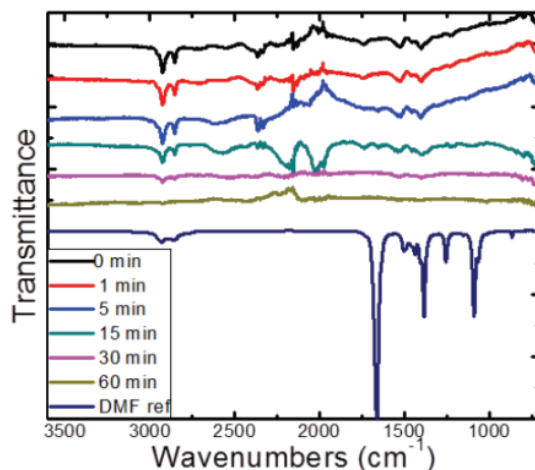


Figure 1.3: (adapted from 39) FTIR of a PbSe-OA thin film in DMF.

The oleic acid ligands, however, were removed after the PbSe-OA QD film was treated with DMF for a period of 15 minutes<sup>39</sup> due to the absence of C-H (OA) absorption peaks near 2674 cm<sup>-1</sup> and 2952 cm<sup>-1</sup>. The adsorption of DMF on PbSe can

be analyzed using DFT simulations. It is unknown if the adsorption of DMF occurs when it is oriented normal to the PbSe surface and if DMF binds to PbSe when positioned parallel to the surface. The adsorption of PbAA<sub>2</sub> on PbSe in DMF will be studied using DFT to confirm FTIR results and show that DMF removes acetic acid, which is a carboxylic acid that compares similarly in binding strength with oleic acid.<sup>2</sup>

### 1.3 Computational Methods

#### 1.3.1 Density Functional Theory

The adsorption of ligands on PbSe and PbS surfaces and surface configuration energies of PbSe and PbS were investigated using DFT and the projector-augmented wave method implemented in Vienna *ab initio* simulation package[21, 22] (VASP). DFT calculations provided the ground-state energies of the investigated structures. The binding energies ( $E_{b,hkl}$ ) of ligands on {hkl} PbSe and PbS surfaces were found using equation 1.[2]

$$E_{b,hkl} = (E_{PbX\{hkl\}} + E_{ligand}) - E_{ligand/PbX\{hkl\}} \quad (1)$$

The ground-state energy of the ligand ( $E_{ligand}$ ), slab ( $E_{PbX\{hkl\}}$ ), and ligand on slab ( $E_{ligand/PbX\{hkl\}}$ ) were determined after forces and stress tensors were used to relax structures in VASP and after a minimum energy was obtained.[23] A positive  $E_{b,hkl}$  value indicates a molecule adsorbing favorably on the surface, whereas a negative binding energy signifies a molecule unbound in the system.[2] Accurate solvation binding energies were obtained from equation 1 after the linear polarization model[24] was applied to relaxed structures in DFT simulations. The linear polarization model uses a generalized Poisson-Boltzmann equation[24] shown below,

$$\vec{\nabla} \cdot (\epsilon(\mathbf{r}) \vec{\nabla} \phi(\mathbf{r})) = -4\pi n(\mathbf{r}) \quad (2)$$

where  $\phi(\mathbf{r})$  represents the electrostatic potential, and  $n(\mathbf{r})$  represents the total electron density of the system.[24] Equation 2 accounts for the electrostatic interactions of ligands and crystal structures in a solvent medium when the relative permittivity ( $\epsilon$ ) is specified in VASP.

### 1.3.2 Ligand Binding Energies

The binding energies of one DMF and two DMF ligands were calculated for larger {100} PbSe and {100} PbS surfaces comprising of 80 atoms (40 Pb–40 X; X=Se,S), five layers, and a vacuum region of 12 Å with surface area dimensions of 12.41 × 12.41 Å for PbSe and 11.98 × 11.98 Å for PbS. For PbAA<sub>2</sub> ligands and more than three DMF ligands, a {100} PbSe slab with a total of 125 atoms (63 Se–62 Pb), five layers, and a 2.88 nm<sup>2</sup> surface area in a vacuum of 12 Å was used. The systems that were constructed to analyze two DMF ligands were used to analyze the adsorption of hydrazine, dithiolane, and lead chloride on PbSe and PbS surfaces. The coordinates of each structure were obtained from Avogadro software[23] and Atomistic Simulation Environment 3.60 (ASE)[25] software and visualized in Visualization for Electronic and Structural Analysis[26] (VESTA) program. All calculations were performed using the Perdew-Burke Ernzerhof projector augmented-wave (PBE-PAW) exchange-correlation functional.[27, 28] A PbSe lattice constant parameter,  $a_0$  of 6.205 Å and a PbS lattice constant parameter of 5.993 Å was obtained by first converging the cutoff energy to find the lowest energy at a specific  $a_0$  and then relaxing the unit cell volume in VASP (see Table S1-S3 in Appendix).

### 1.3.3 Crystal Structure Coordinates

The crystal structure coordinates of PbSe and PbS were obtained from Avogadro software. The coordinates of all investigated ligands were obtained from Avogadro software. The PbSe and PbS slabs were constructed using Atomistic Simulation Environment 3.60 (ASE)[25] and a supercell program. In a  $1 \times 1 \times 1$  conventional unit cell, PbSe and PbS have a total of 8 atoms. Before ab initio simulations, ligands were individually positioned 2.8 – 3.5 Å above PbX surfaces.

### 1.3.4 Convergence Tests

PbSe and PbS cutoff energies were determined using bulk structures and performing energy convergence tests. The energy convergence tests started with the highest cutoff energy found in PbSe or PbS atoms and finalized when energy convergence was satisfied. During relaxations and convergence tests, the ground-state energies were converged to less than 1 meV/atom. A conventional unit cell having a total of eight atoms was used to determine the cutoff energies for PbSe and PbS slabs. The conventional unit cell of PbSe converged at 400 eV, and the conventional unit cell of PbS converged at a cutoff energy of 450 eV. Convergence tests were performed on  $k$ -point meshes to sample the Brillouin zone (reciprocal primitive cell) and determine  $k$ -point densities for PbS and PbSe slabs. A  $k$ -point density of 60 per Å<sup>-1</sup> was observed for PbSe and PbS conventional cells. The automatic  $k$ -mesh generation was employed, and the Gamma-centered  $k$ -point meshes were  $5 \times 5 \times 1$  for {100} PbSe and PbS surfaces,  $4 \times 4 \times 1$  for {110} PbSe (50 Pb–50 Se atoms) surfaces, and  $3 \times 4 \times 1$  for reconstructed {111} PbSe (48 Pb–48 Se atoms) surfaces. One  $k$ -point ( $1 \times 1 \times 1$ ) was used for ligands in bulk. In addition, the top two layers of the PbSe and PbS slabs

were only allowed to relax, and  $E_{b,hkl}$  was calculated by applying a cutoff energy of 550 eV in ligands, slabs, and ligand on slab structures. Soft PBE-PAW exchange correlation functionals were used in all ligands to obtain low convergence cutoff energies. Dimethylformamide was relaxed in a volume with dimensions  $13 \times 13 \times 13$  Å using soft pseudopotentials and a cutoff energy of 500 eV. Relaxations of the ligands on PbX surfaces were performed using a cutoff energy of 550 eV. Different Monkhorst-Pack  $k$ -point meshes were applied to ligands on PbX surface models (see Table S2). The convergence criterion used for electronic relaxations was less than 1 meV/atom. Table S4 in the Appendix section shows the permittivity values applied to all structures in DFT calculations to account for solvent effects.

### 1.3.5 Stable Configurations

Figure 4 illustrates different PbAA<sub>2</sub> configurations on {100} PbSe surfaces. Several PbAA<sub>2</sub> geometries were analyzed in VASP to determine the most stable configuration of PbAA<sub>2</sub> on {100} PbSe and understand how PbAA<sub>2</sub> binds to PbSe surfaces. Figure 1.4-b represents the configuration of PbAA<sub>2</sub> that binds strongly to PbSe because the oxygen atoms of PbAA<sub>2</sub> interact with Pb surface atoms.

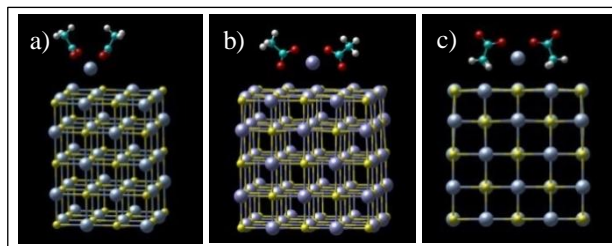


Figure 1.4: PbAA<sub>2</sub> on {100} PbSe surfaces. a)  $E_b = 0.24$  eV (vacuum). b)  $E_b = 0.42$  eV (vacuum),  $E_b = -0.12$  eV (in DMF medium). c)  $E_b = 0.30$  eV (vacuum). Pb in gray blue; Se in yellow; O in red; C in cyan; H in white.

### 1.3.6 Solvation Surface Energies

The solvation surface energies of PbS and PbSe surfaces were calculated by applying the linear polarization solvent model<sup>26</sup> on bulk PbSe and PbS structures. A bulk energy,  $E_{\text{bulk}}$  of  $-4.11$  eV/atom was obtained for PbSe in vacuum. The bulk energy of PbS in vacuum was approximately  $-4.40$  eV/atom. The linear polarization solvent model was applied to relaxed slabs that had a vacuum spacing that ranged  $10\text{--}14$  Å (see Fig. 1.5).

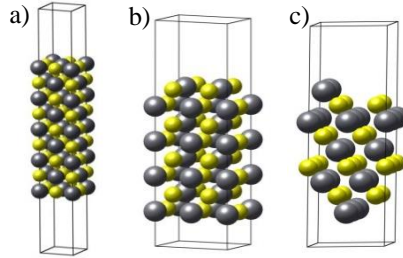


Figure 1.5: Illustration of PbX slabs. a)  $\{100\}$  PbX. PbSe:  $6.205$  Å  $\times$   $6.205$  Å; PbS:  $5.993$  Å  $\times$   $5.993$  Å. b)  $\{110\}$  PbX. PbSe:  $8.775$  Å  $\times$   $6.205$  Å; PbS:  $8.476$  Å  $\times$   $5.993$  Å. c)  $\{111\}$  PbX. PbSe:  $8.775$  Å  $\times$   $8.775$  Å; PbS:  $8.476$  Å  $\times$   $8.476$  Å.

The  $\{100\}$  slabs contained 9 layers, while the  $\{110\}$  and nonpolar  $\{111\}$  slabs had 8 layers (2 Pb–2 X per layer; X=Se,S). The Gamma-centered  $k$ -point meshes were  $10 \times 10 \times 1$ ,  $7 \times 10 \times 1$ , and  $8 \times 8 \times 1$  for  $\{100\}$ ,  $\{110\}$ , and nonpolar  $\{111\}$  surfaces, respectively, and equation 3 was used to evaluate surface energies<sup>2</sup> ( $\gamma_{\text{hkl}}$ ),

$$\gamma_{\text{hkl}} = \frac{E_{\text{PbX}\{\text{hkl}\}} - NE_{\text{bulk}}}{2A} \quad (3)$$

where  $N$  is the number of atoms in the system and  $A$  is the facet area. An area of  $\sqrt{2}a_0 \times a_0$  was used to calculate  $\gamma_{110}$ . The area used to calculate the surface area for a  $\{100\}$  facet was  $a_0^2$ , and the area used to calculate  $\gamma_{111}$  was  $\sqrt{3}a_0 \times a_0$ .

## 1.4 Results

### 1.4.1 Binding Energies

The binding energies of  $\text{PbCl}_2$  on  $\{100\}$  PbS and  $\text{PbAA}_2$ ,  $\text{N}_2\text{H}_4$ , and  $\text{C}_3\text{H}_6\text{S}_2$  separately on  $\{100\}$  PbSe surfaces in the presence of solvent medium are shown in Figures 1.6 a-b.

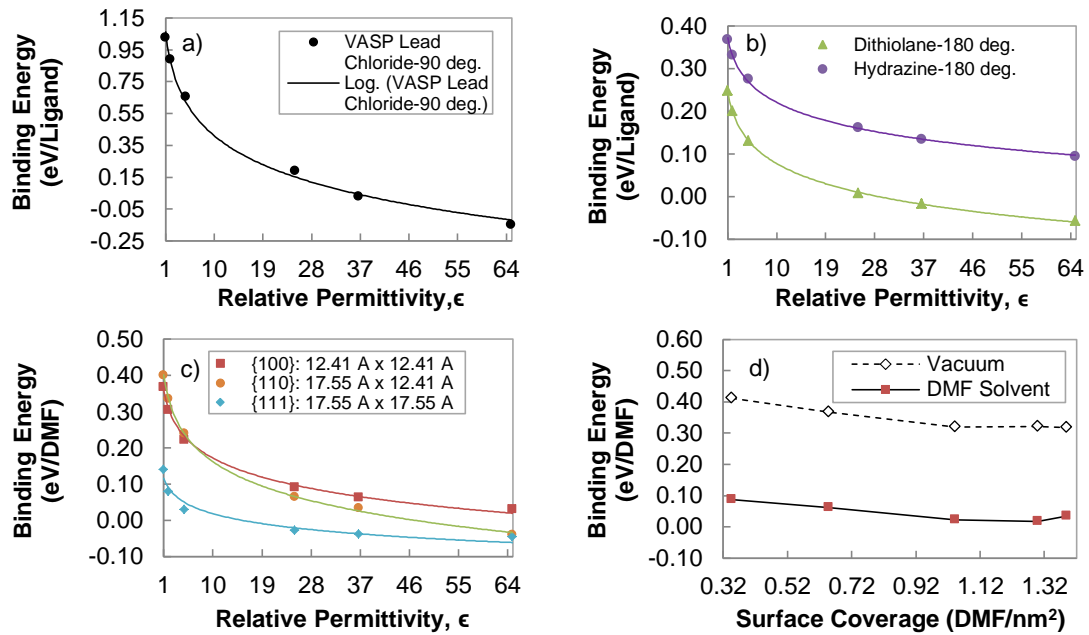


Figure 1.6: Binding energy plotted against  $\epsilon$  for a)  $\text{PbCl}_2$  on  $\{100\}$  PbS, b) organic ligands on  $\{100\}$  PbSe, and c) DMF on PbSe surfaces,  $\theta=90^\circ$ . d) Binding energy plotted against surface coverage for  $\{100\}$  PbSe surface,  $\theta=90^\circ$ .

The data reveals a reduction in binding energy as  $\epsilon$  increases and shows the polar solvents affecting the adsorption of the ligand on PbSe or PbS surface. The high-polar solvents lead to the desorption of the ligand from the PbSe or PbS surface, which can

be confirmed with negative  $E_b$  values. The ligands were not adsorbed to PbS and PbSe surfaces in solvents with large dipole moments due to strong electrostatic interactions between solvents and ligands. Hydrazine has an  $E_b$  of 0.37 eV on {100} PbS in vacuum (Fig. 1.6-b), which is slightly higher than Kutana's<sup>21</sup> result for N<sub>2</sub>H<sub>4</sub> on {100} PbSe ( $E_b = 0.34$  eV). An  $E_b$  of 0.24 eV and 0.42 eV was found for a coverage of 1.30 AA<sup>-</sup>/nm<sup>2</sup> (Fig. 1.5-a) and 0.70 AA<sup>-</sup>/nm<sup>2</sup> (Fig. 1.5-b), respectively on {100} PbSe. Bealing et al.<sup>2</sup> obtained an  $E_b$  value of 0.87 eV for a coverage of 0.75 AA<sup>-</sup>/nm<sup>2</sup> and 0.52 eV for a coverage of 1.30 AA<sup>-</sup>/nm<sup>2</sup> on {100} PbSe surface.

Figure 1.6-c also has similar characteristics as Figures 1.6 a–b. Lower ground-state energies were observed in all ligands, slabs, and ligand-slab structures when  $\epsilon$  was increased due to electrostatic interactions between structures and solvents. The adsorption of DMF on {100} PbSe and {110} PbSe were similar at low  $\epsilon$  values, but lower DMF binding energies were obtained on {111} PbSe (Fig. 1.6-c). Figure 1.6-d shows  $E_b$  decreasing with surface coverage for DMF, and Figure 1.7 illustrates DMF at different positions and orientations on PbSe. VASP results indicate DMF binding strongly to {100} PbSe and {100} PbS surfaces in vacuum when positioned normal to the surface (Fig. 1.7-b) and binding less strongly to PbSe and PbS surfaces in DMF medium.

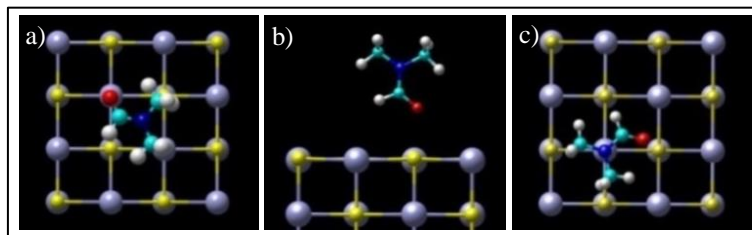


Figure 1.7: DMF adsorbed on {100} PbSe surface in vacuum with an  $E_b$  of a) 0.22 eV,  $E_{b,DMF} = -0.16$  eV for O(DMF)-Pb(PbSe) [ $\theta = 180^\circ$ ], distance difference,  $d = 2.93$  Å, b) 0.37 eV,  $E_{b,DMF} = 0.062$  eV for O(DMF)-Pb(PbSe) [ $\theta = 90^\circ$ ],  $d = 2.81$  Å, and c) 0.023 eV,  $E_{b,DMF} = -0.21$  eV for N(DMF)-Pb(PbSe) [ $\theta = 180^\circ$ ],  $d = 2.88$  Å. Pb in gray blue; N in blue; C in cyan; H in white; O in red; Se in yellow. {100} PbS surface: a)  $E_b = 0.21$  eV,  $E_{b,DMF} = -0.17$  eV. b)  $E_b = 0.32$  eV,  $E_{b,DMF} = 0.033$  eV. c)  $E_b = -0.022$  eV,  $E_{b,DMF} = -0.40$  eV ( $d = 2.90$  Å for cases a-c in PbS surface).

## 1.4.2 Solvation Surface Energies

Figure 1.8 reports the solvation surface energies for three PbSe and PbS facets and compares the surface energies in DMF with those in vacuum. Using the PBE functional, the energy ordering of the facets is  $\gamma_{100} < \gamma_{110} < \gamma_{111}$  for PbSe and PbS surfaces. The solvation surface energies of PbSe are relatively similar to the solvation surface energies of PbS but are lower than the surface energies of PbSe in vacuum. A decrease in surface energy is also observed for PbS in DMF.

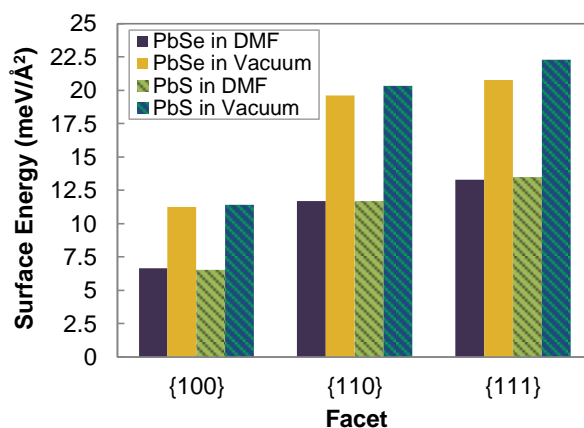


Figure 1.8: PbSe and PbS Solvation Surface Energies.

Figures 1.9 and 1.10 report the solvation surface energies for three PbSe and PbS facets and compares the surface energies in various solvents with those in vacuum. Using the PBE functional, the energy ordering of the facets is  $\gamma_{100} < \gamma_{110} < \gamma_{111}$  for PbSe and PbS surfaces. The solvation surface energies of PbSe are relatively similar to the solvation surface energies of PbS but are lower than the surface energies of PbSe in vacuum.

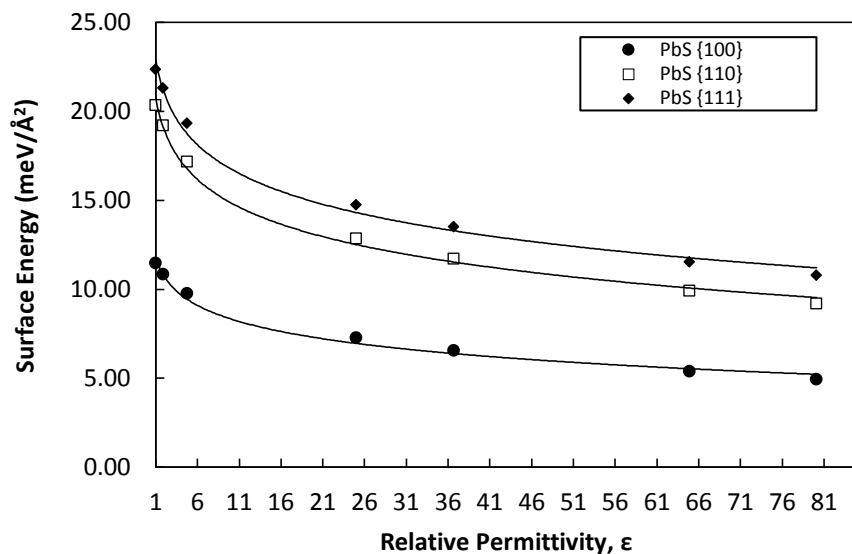


Figure 1.9: Surface energy of (100), (110), and (111) PbS facets changing with relative permittivity.

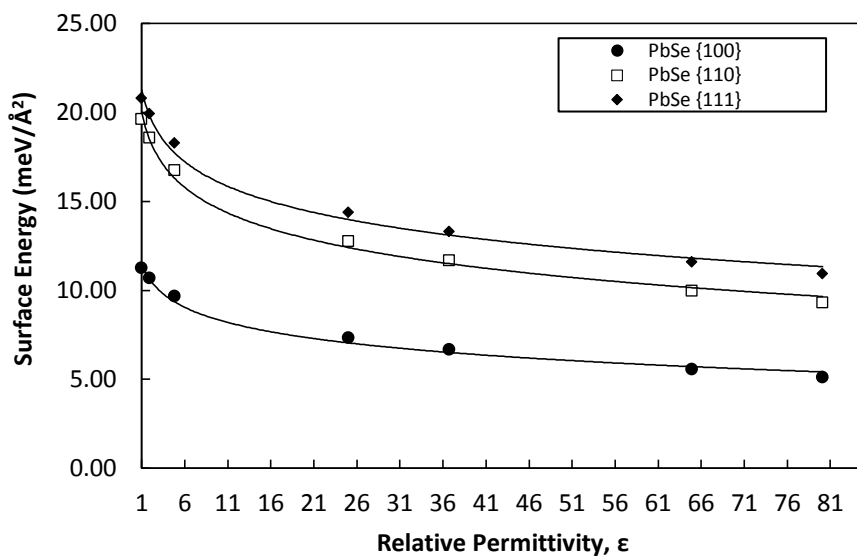


Figure 1.10: Surface energy of (100), (110), and (111) PbSe facets changing with relative permittivity.

Figure 1.9 and 1.10 also illustrate the surface energy of the PbSe and PbS facets decreasing logarithmically as the relative permittivity increases. We developed an empirical model for the solvation surface energy of PbSe and PbS. Equation 4 is the

solvation surface energy of a material with hkl indices as a function of relative permittivity,  $\varepsilon$

$$\gamma_{hkl}(\varepsilon) = -A \ln(\varepsilon) + B \quad (4)$$

where A and B are fitting parameters. Parameter B represents the surface energy of {hkl} facet material at vacuum conditions ( $\varepsilon = 1$ ). As relative permittivity increases to values  $\varepsilon > 1$ , the surface energy of the material decreases.

$$\frac{d\gamma_{hkl}(\varepsilon)}{d\varepsilon} = -\frac{A}{\varepsilon} \quad (5)$$

$$\lim_{\varepsilon \rightarrow \infty} \frac{d\gamma_{hkl}(\varepsilon)}{d\varepsilon} = 0 \quad (6)$$

As the limit of  $\varepsilon$  approaches infinity ( $\varepsilon \rightarrow \infty$ ), the surface energy of the material reaches a minimum value,  $\gamma_{hkl, \min}(\varepsilon)$ . From DFT calculations, we note that the fitting parameters vary with {hkl} facet of PbSe and PbS. The fitting parameters determined for the surface energy of PbSe facets were similar but not equal to the fitting parameters of PbS surface energy expression. The following fitting parameters were obtained for PbSe and PbS facets shown in Table 1.1.

Table 1.1: Fitting parameters for calculating solvation surface energy of PbS and PbSe facets.

Facet	Fitting Parameters			
	$A_{PbS}$	$A_{PbSe}$	$B_{PbS}$	$B_{PbSe}$
(100)	1.50	1.40	11.77	11.55
(110)	2.56	2.36	20.75	20.02
(111)	2.67	2.27	22.90	21.29

## 1.5 Research Plan

### 1.5.1 Monofunctional and Bifunctional Ligands

Accurate binding energies for  $\text{PbAA}_2$  on  $\{100\}$ ,  $\{110\}$ , and nonpolar  $\{111\}$  PbS and PbSe surfaces in vacuum and solvents will continue to be determined. A new model will be proposed for binding energy when solvents are accounted in which  $E_b$  will depend on the surface coverage and the permittivity.<sup>2</sup> Another group of ligands are dicarboxylic acids (bifunctional ligands). These ligands can be studied in VASP to examine their adsorption strength on PbSe and PbS surfaces in solvents. We propose to study lead oxalate, lead fumarate, and lead maleate ligands on PbSe and PbS surfaces.<sup>35</sup> The first approach will be to construct the ligand by binding the dianion of the dicarboxylic acid with a Pb atom in bridging or chelating mode.<sup>2,35</sup> The next step will be to position the ligands above Pb surface atoms using XMakeMol<sup>50</sup> software. Chelating and bridging modes will be analyzed to determine binding energy differences in each configuration, and the binding energies will be compared to the binding energies of  $\text{PbAA}_2$  on PbS and PbSe surfaces.

### 1.5.2 Analysis of Ligand Binding

The adsorption of  $\text{PbAA}_2$  and DMF on  $\{100\}$ ,  $\{110\}$ , and nonpolar  $\{111\}$  lead chalcogenide surfaces in vacuum and solvents can be studied further by applying Bader charge analysis.<sup>37</sup> The charge of lead surface atoms will be compared before ligand adsorption and after ligand adsorption to identify the atom in the ligand that mostly transfers electrons to  $\text{PbX}$  ( $\text{X}=\text{S},\text{Se}$ ) surfaces. The Bader charge algorithm is integrated into VASP by obtaining the Bader analysis program from the Henkelman Research Group at the University of Texas at Austin.<sup>42</sup> Electron accumulation in the

ligand-slab system will be visualized by obtaining the highest occupied molecular orbitals (HOMO) and lowest unoccupied molecular orbitals (LUMO)<sup>51</sup> from Bader charge data in XCrySDen<sup>52</sup> software. The local density of states (projected DOS) of the relaxed ligand-slab structure will also be obtained from VASP<sup>42</sup> to determine the effect of ligands on the electronic structure of PbX by following Lee<sup>42</sup> methodology where the number of states per unit cell and the projected orbitals of each band will be used to obtain the energy levels and occupancies at each orbital.

### 1.5.3 Silver Doped PbSe Surfaces

Having analyzed binding energies of various ligands on lead chalcogenide surfaces in solvent medium, the next step will be to study the effects of doping on electronic properties in PbSe. “Heavy doping” of lead chalcogenide nanocrystals is a challenge due to the difficulty of introducing multiple charges consistently into quantum-confined band-edge states.<sup>22</sup> The effects of silver (Ag) doping on PbSe surfaces on the adsorption energy of tetracyanoquinodimethane [(NC)<sub>2</sub>CC<sub>6</sub>H<sub>4</sub>C(CN)<sub>2</sub>] will be investigated in VASP.<sup>51,53</sup> The adsorption energy of tetracyanoquinodimethane will be studied and compared to DMF as a function of Ag concentration.<sup>51,53</sup> Structures will be prepared in Avogadro software. Density of states (DOS) for intrinsic PbSe and Ag-doped PbSe will be obtained from VASP by using a denser *k*-point grid and increasing the convergence criterion.<sup>42,54</sup> Furthermore, adsorption energy equations studied by Xu et al.<sup>51</sup> will be modified and applied to the proposed systems in order to compare adsorption energies of organic adsorbates on Ag-doped PbSe surfaces to adsorption energies of organic adsorbates on intrinsic PbSe surfaces.

#### 1.5.4 Surface Oxidation on PbSe Nanocrystals

The adsorption of oxygen on {100}, {110}, and nonpolar {111} PbSe surfaces will be explored in VASP.<sup>55</sup> The purpose of studying oxygen adsorption on PbSe surfaces is to observe changes in PbSe structure and determine the lowest energy binding structures after oxidation.<sup>55</sup> PbSe surfaces will be constructed in ASE, and the O<sub>2</sub> molecules as well as the O atoms will be placed at random locations above the topmost atom of the surfaces in Avogadro software.<sup>22</sup> The next step will be to explore the dynamics of oxidation in PbSe nanocrystals using Large-scale Atomic/Molecular Massively Parallel Simulator<sup>56</sup> (LAMMPS) software. To accurately model chemical reactions in this project, the reactive force field interatomic potential (ReaxFF) will be used.<sup>2</sup> For computational efficiency, the oxidation of {100}, {111}, and {110} PbSe surfaces will be simulated first in LAMMPS, and atomic configurations will be obtained using Visualization Molecular Dynamics<sup>57</sup> (VMD) program. A PbSe nanocrystal will be modeled in the shape of a cube-octahedral.<sup>34</sup> A Fortran code will be created to position alkyl amine ligands on PbSe surfaces and O atoms in vacuum. The surface oxidation of PbSe nanocrystals will be investigated at 298 K for a constant volume, pressure, and temperature (NVT) system. MD simulations will run until thermodynamic equilibrium is satisfied.<sup>25</sup> The radial distribution functions (RDF) will be obtained from LAMMPS to analyze the interactions between oxygen and surface PbSe atoms,<sup>2</sup> and the nanocrystal structure will be visualized in VMD to note any shape changes.

#### 1.6 Conclusion

The integration of the solvation model in *ab-initio* density functional theory calculations allowed further studies of the effect of solvents in facet surface energies

and the adsorption of ligands on nanocrystal facets. In this study, lead sulfide and lead selenide nanocrystal facets were constructed to determine ligand solvation binding energies and determine solvation surface energies. Based on the studies performed using VASP and the solvation model, surface energies as well as ligand binding energies changed as a function of the dielectric constant of the solvent medium. Solvents with higher dielectric constants significantly reduced surface facet energies and ligand binding energies. Low dielectric constant solvents, on the other hand, did not have a significant impact on surface energies and ligand binding energies when compared to vacuum system models. Both solvation surface energies and solvation ligand binding energies demonstrated a logarithmic decrease behavior as the dielectric constant increased with respect to the vacuum system ( $\epsilon=1$ ).

## REFERENCES

1. Inerbaev, T. M., Masunov, A. E., Khondaker, S. I., et al., “Quantum chemistry of quantum dots: Effects of ligands and oxidation”, *J. Chem. Phys.* **131**, 044106 (2009).
2. Bealing, C. R., Baumgardner, W. J., Choi, J. J., Hanrath, T. & Hennig, R. G., “Predicting nanocrystal shape through consideration of surface ligand interactions”, *ACS Nano* **6**, 2118–2127 (2012).
3. Choi, J. J., Wenger, W. N., Hoffman, R. S., Lim, Y., Luria, J., Jasieniak, J., Marohn, J. A. & Hanrath, T., “Solution-processed nanocrystal quantum dot tandem solar cells”, *Advanced Materials* **23**, 3144–3148 (2011).
4. Moreels, I., Lambert, K., Smeets, D., De Muynck, D., Nollet, T., Martins, J. C., Vanhaecke, F., et al., “Size-dependent optical properties of colloidal PbS quantum dots”, *ACS Nano* **3**, 10, 3023–30 (2009).
5. Lingley, Z., Lu, S. & Madhukar, A., “A high quantum efficiency preserving approach to ligand exchange on lead sulfide quantum dots and interdot resonant energy transfer”, *Nano Letters* **11**, 2887–2891 (2011).
6. Choi, J. J., Lim, Y., Santiago-Berrios, M. B., Oh, M., Hyun, B., Sun, L., Bartnik, A. C., et al., “PbSe nanocrystal excitonic solar cells”, *Nano Letters* **9**, 3749–3755 (2009).
7. Law, M., Luther, J. M., Song, Q., Hughes, B. K., Perkins, C. L. & Nozik, A. J., “Structural, optical, and electrical properties of PbSe nanocrystal solids treated thermally or with simple amines”, *J. Am. Chem. Soc.* **130**, 5974–5985 (2008).
8. Gray, J. L., “The Physics of the Solar Cell”, *Handbook of Photovoltaic Science and Engineering*, Second Edition (eds A. Luque and S. Hegedus), John Wiley & Sons, Ltd, Chichester, UK (2011).
9. Aroutiounian, V., Petrosyan, S., Khachatryan, A. & Touryan, K., “Quantum dot solar cells”, *Journal of Applied Physics* **89**, 2268–2271 (2001).
10. Moreels, I., Fritzing, B., Martins, J. C. & Hens, Z., “Surface Chemistry of Colloidal PbSe Nanocrystals”, *J. Am. Chem. Soc.* **130**, 15081–15086 (2008).
11. Fu, H., Luan, W. & Tu, S., “A simple route for synthesis of PbSe nanocrystals: shape control by ligand and reaction time”, *Dalton Transactions* **41**, 12254–12258 (2012).

12. Parak, W. J., Gerion, D., Pellegrino, T., Zanchet, D., Micheel, C., Williams, S. C., Boudreau, R., et al., “Biological applications of colloidal nanocrystals”, *Nanotechnology* **14**, R15-R27 (2003).
13. Choi, J. J., Bealing, C. R., Bian, K., Hughes, K. J., Zhang, W., et al., “Controlling nanocrystal superlattice symmetry and shape anisotropic interactions through variable ligand surface coverage”, *Journal of the American Chemical Society* **133**, 3131–3138 (2011).
14. Kuo, C., Su M., Ku, C., Wang, S., Lee, H. & Wei, K., “Ligands affect the crystal structure and photovoltaic performance of thin films of PbSe quantum dots”, *J. Mater. Chem.* **21**, 11605–11612 (2011).
15. Jawaid, A. M., Asunskis, D. J. & Snee, P. T., “Shape-controlled colloidal synthesis of rock-salt lead selenide nanocrystals”, *ACS Nano* **5**, 6465–6471 (2011).
16. Wang, Y., Tang, A., Li, K., Yang, C., Wang, M., Ye, H., Hou, Y., et al., “Shape-controlled synthesis of PbS nanocrystals via a simple one-step process”, *Langmuir : the ACS journal of surfaces and colloids* **28**, 47, 16436–43 (2012).
17. Pintilie, L., Pentia, E., Matei, I., Pintilie, I. & Ozbay, E., “Field-effect-assisted photoconductivity in PbS films deposited on silicon dioxide”, *Journal of Applied Physics* **91**, 9, 5782-6 (2002).
18. Schaller, R. D., Crooker, S. A., Bussian, D. A., Pietryga, J. M., Joo, J. & Klimov, V. I., “Revealing the Exciton Fine Structure of PbSe Nanocrystal Quantum Dots Using Optical Spectroscopy in High Magnetic Fields”, *Physical Review Letters* **105**, 6, 067403 (2010).
19. Tisdale, W. A. & Zhu, X., “Artificial atoms on semiconductor surfaces”, *Proceedings of the National Academy of Sciences* **108**, 3, 965–970, (2010).
20. Dvorak, M., Wei, S. & Wu, Z., “Origin of the Variation of Exciton Binding Energy in Semiconductors”, *Physical Review Letters* **110**, 016402, 1–5 (2013).
21. Kutana, A. & Erwin, S. C., “PbSe nanocrystals remain intrinsic after surface adsorption of hydrazine”, *Physical Review B* **83**, 235419 (2011).
22. Koh, W., Kuposov, A. Y., Stewart, J. T., Pal, B. N., Robel, I., Pietryga, J. M. & Klimov, V. I., “Heavily doped n-type PbSe and PbS nanocrystals using ground-state charge transfer from cobaltocene”, *Scientific Reports* **3**, 2004 (2013).
23. Kohn, W., Becke, A. D. & Parr, R. G., “Density Functional Theory of Electronic Structure”, *J. Phys. Chem.* **100**, 96, 12974–12980 (1996).

24. Jariwala, B. N., Ciobanu, C. V. & Agarwal, S., “Initial oxidation stages of hydrogen-and styrene-terminated Si(100) surfaces: A molecular dynamics study”, *Surface Science* **605**, 21-22, L61–L66 (2011).
25. Binder, K., Horbach, J., Kob, W., Paul, W. & Varnik, F., “Molecular dynamics simulations”, *Journal of Physics: Condensed Matter* **16**, 5, S429–S453 (2004).
26. Fishman, M., Zhuang, H. L., Mathew, K., Dirschka, W. & Hennig, R. G., “Accuracy of exchange-correlation functionals and effect of solvation on the surface energy of copper”, *Physical Review B* **87**, 24, 245402 (2013).
27. Cramer, C. J. & Truhlar, D. G., “Implicit Solvation Models: Equilibria, Structure, Spectra, and Dynamics”, *Chemical Reviews* **99**, 8, 2161–2200 (1999).
28. Rosen, E. L., Buonsanti, R., Llodes, A., Sawvel, A. M., Milliron, D. J. & Helms, B. A., “Exceptionally mild reactive stripping of native ligands from nanocrystal surfaces by using Meerwein’s salt”, *Angewandte Chemie International Edition* **51**, 3, 684–9 (2012).
29. Yildiz, I., Ray, S., Benelli T. & Raymo, F. M., “Dithiolane ligands for semiconductor quantum dots”, *J. Mater. Chem.* **18**, 33, 3940–3947 (2008).
30. Ip, A. H., Thon, S. M., Hoogland, S., Voznyy, O., Zhitomirsky, D., et al., “Hybrid passivated colloidal quantum dot solids”, *Nature Technology* **7**, 577–582 (2012).
31. Fang, C., van Huis, M. A., Vanmaekelbergh, D. & Zandbergen, H. W., “Energetics of polar and nonpolar facets of PbSe nanocrystals from theory and experiment”, *ACS Nano* **4**, 211–218 (2010).
32. Dai, Q., Zhang, Y., Wang, Y., Wang, Y., Zou, B., Yu, W. W. & Hu, M. Z., “Ligand Effects on Synthesis and Post-Synthetic Stability of PbSe Nanocrystals”, *The Journal of Physical Chemistry C* **114**, 39, 16160–16167 (2010).
33. Zarghami, M. H., Liu, Y., Gibbs, M., Gebremichael, E., Webster, C. & Law, M., “p-Type PbSe and PbS Quantum Dot Solids Prepared with Short-Chain Acids and Diacids”, *ACS Nano* **4**, 4, 2475–2485 (2010).
34. Kaushik, A. P. & Clancy, P., “Explicit all-atom modeling of realistically sized ligand-capped nanocrystals”, *The Journal of Chemical Physics* **136**, 11, 114702 (2012).
35. Smith, A. R., Yoon, W., Heuer, W. B., Baril, S. I. M., Boercker, J. E., Tischler, J. G. & Foos, E. E., “Effect of Ligand Structure on the Optical and Electronic Properties of Nanocrystalline PbSe Films”, *The Journal of Physical Chemistry C* **116**, 10, 6031–6037 (2012).

36. Robert C. & Melvin J. A., “CRC Handbook of Chemistry and Physics”, 64th Edition, Editor in Chief R. C. Weast, CRC Press Inc., Boca Raton, Florida (1983).
37. Tang, W., Sanville E. & Henkelman G., “A grid-based Bader analysis algorithm without lattice bias”, *J. Phys.: Condens. Matter* **21**, 084204 (2009).
38. Pastoriza-Santos, I. & Liz-Marzán, L. M., “N, N-Dimethylformamide as a Reaction Medium for Metal Nanoparticle Synthesis”, *Advanced Functional Materials* **19**, 679–688 (2009).
39. Baumgardner, W., Whitham, K. & Hanrath T., “Confined-but-Connected Quantum Solids Via Controlled Ligand Displacement”, *Nano Letters* **13**, 7, 3225–3231 (2013).
40. Kresse, G. & Furthmüller, J., “Efficient iterative schemes for ab initio total-energy calculations using a plane-wave basis set”, *Physical Review B, Condensed Matter* **54**,16, 11169–11186 (1996).
41. Kresse, G. & Joubert, D., "From ultrasoft pseudopotentials to the projector augmented-wave method", *Physical Review B* **59**, 3, 11–19 (1999).
42. Lee, J. G. *Computational Materials Science: An Introduction*. Ed. CRC Press, Taylor & Francis, Boca Raton, FL, 197-250 (2011).
43. Avogadro. [http://avogadro.openmolecules.net/wiki/Main\\_Page](http://avogadro.openmolecules.net/wiki/Main_Page).
44. Atomistic Simulation Environment. <http://wiki.fysik.dtu.dk/ase/index.html>.
45. Momma, K. & Izumi, F., “VESTA: a three-dimensional visualization system for electronic and structural analysis”, *Journal of Applied Crystallography* **41**, 3, 653–658 (2008).
46. Paier, J., Hirschl, R., Marsman, M. & Kresse, G., “The Perdew-Burke-Ernzerhof exchange-correlation functional applied to the G2-1 test set using a plane-wave basis set”, *The Journal of Chemical Physics* **122**, 23, 234102 (2005).
47. Ernzerhof, M. & Scuseria, G. E., “Assessment of the Perdew–Burke–Ernzerhof exchange-correlation functional”, *The Journal of Chemical Physics* **110**, 11, 5029–5036 (1999).
48. Ashcroft, N. W. & Mermin D. N. *Solid State Physics*. Thomson Learning Inc., Glendale, CA. (1976).

49. Troullier N. & Martins, J. L., “Efficient pseudopotentials for plane-wave calculations”, *Physical Review B* **43**, 3, 1993-2006 (1991).
50. XMacemol. <http://www.nongnu.org/xmakemol>.
51. Xu, Y., Hofmann, O. T., Schlesinger, R., Winkler, S., Frisch, J., Niederhausen, J., Vollmer, A., et al., “Space Charge Transfer in Hybrid Inorganic/Organic Systems”, *Journals of the American Physical Society* 1–5 (2013). arXiv:1306.4508.
52. Kokalj, A., “XCrySDen—a new program for displaying crystalline structures and electron densities”, *Journal of Molecular Graphics & Modelling* **17**, 176–9, 215–6 (2000).
53. Kang, M. S., Sahu, A., Frisbie, C. D. & Norris, D. J., “Influence of silver doping on electron transport in thin films of PbSe nanocrystals”, *Advanced Materials* **25**, 5, 725–31 (2013).
54. Raymand, D., Jacobsson, T. J., Hermansson, K. & Edvinsson, T., “Investigation of Vibrational Modes and Phonon Density of States in ZnO Quantum Dots”, *The Journal of Physical Chemistry C* **116**, 12, 6893–6901 (2012).
55. Mastail, C., Bourennane, I., Estève, A., Landa, G., Rouhani, M. D., Richard, N. & Hémercyck, A., “Oxidation of Germanium and Silicon surfaces (100): a comparative study through DFT methodology”, *IOP Conference Series: Materials Science and Engineering* **41**, 012007 (2012).
56. LAMMPS. <http://lammps.sandia.gov>.
57. Humphrey, W., Dalke, A. & Schulten, K., “VMD: visual molecular dynamics”, *Journal of Molecular Graphics* **14**, 1, 33–8, 27–8 (1996).

## CHAPTER 2

### PHOTONIC CRYSTALS

#### 2.1 Introduction

Photonic crystals have a periodic refractive index in one dimension, two dimensions, quasi-two dimensions (slab), or three dimensions.<sup>1</sup> The periodicity of refractive index in 1D, 2D, and 3D in photonic crystals is modeled in Figure 2.1.

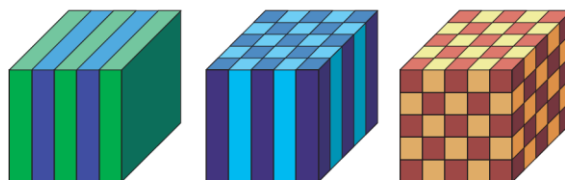


Figure 2.1: Periodic refractive index in 1D, 2D, and 3D. [1]

Photonic crystals can be used for spatial localization as waveguides and resonators. Other applications that photonic crystals can be utilized for include spontaneous emission control for photovoltaic solar cells and lasers, superlens for imaging beyond the diffraction limit, and optical integration and optoelectronics. As of today, challenges remain in fabricating diverse structures with strong light-matter interaction. At the molecular scale complex structures commonly form, ‘programmed’ by the chemical functionality of the constituent groups within molecules.<sup>2</sup> Our aim is toward studies that extend the concepts, which build materials at the molecular scale, to the assembly of objects at the submicron scale. Patchy particle systems which utilize DNA, proteins, or lipid bi-layers to provide direction specific binding between spherical particles have already been reported. Particularly, our approach will ultimately utilize confinement of patchy nonspherical particles for directing the

colloidal assembly and produce mesoscale structures that can allow light control through photonic crystal effects.

### 2.1.1 Patchy Particles

Patchy particles are particles that have interaction “patches” on the surface<sup>3-5</sup> Patchy particles can assemble into different structures depending on the chemical properties of the patches.<sup>2,6-7</sup> Many fabrication techniques have yielded patchy particles, and these fabrication techniques are illustrated in Figure 2.2.

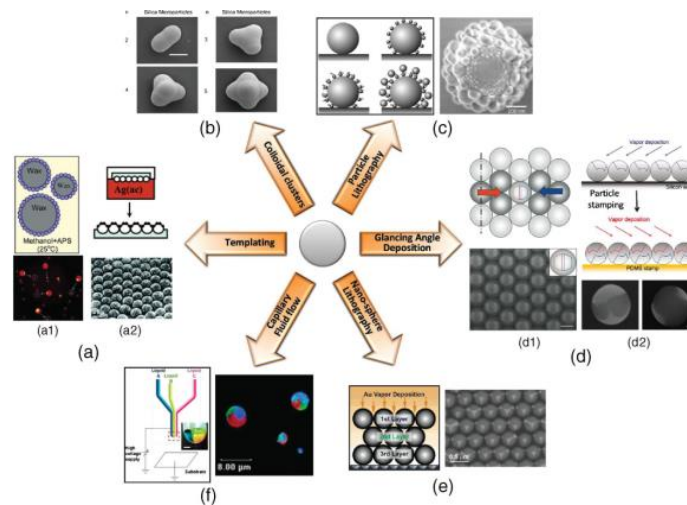


Figure 2.2: Techniques for synthesis and microfabrication of patchy particles. [2]

Techniques for synthesis and microfabrication of patchy particles include templating, colloidal clusters, particle lithography, glancing angle deposition, nano-sphere lithography, and capillary fluid flow.<sup>2</sup> In this study, we mostly focused on using the glancing angle deposition to coat particles with metal thin films. Chen et al.<sup>8</sup> examined the assembly and arrangements of patchy particles using glancing angle deposition. In Chen’s work, silica microparticles were coated with gold and titanium, and the surface

of the patchy particles was modified with a thiol ligand to make the particles hydrophobic.<sup>8</sup> The patchy particles produced by Chen's research work had three different structural patterns. If the particles were coated at an angle of 30 degrees, the particle had a K-bonding geometry after gold etching the gold particles which resulted in a Kagome lattice structure<sup>8</sup> as shown in Figure 2.3. Etching the gold for a period of more than 120 seconds after thin film deposition resulted in a Y-bonding geometry and an hexagonal lattice structure once particles assembled in solution.<sup>8</sup>

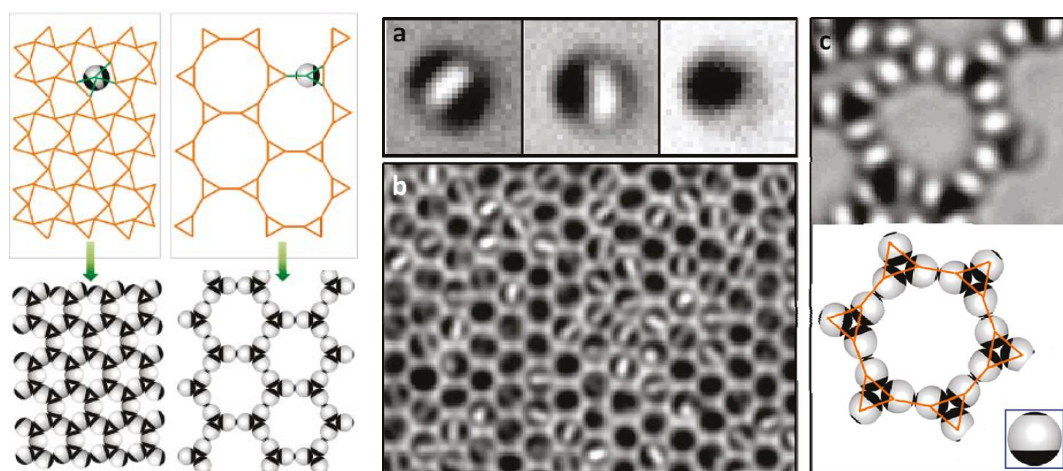


Figure 2.3: (left) Schematic models of distorted Kagome lattice  $3\cdot6\cdot3\cdot6$  and  $3\cdot12^2$ , respectively from building blocks with 'K' and 'Y' bonding geometry.[8] (right). Optical images of hexagonal lattice formed by X-type silica patchy particles.

Patchy particles were fabricated by drop-casting a silica colloidal suspension on a substrate. The monolayer of silica particles was exposed to gold on one side and lifted using an elastomeric stamp. The particles with a silica hemisphere on the top and a gold hemisphere on the lower hemisphere were exposed to gold one more time. The particles were completely covered with gold, and the gold in the particles was etched for a period of time. Based on the gold etching time, Chen and researches observed a change in bonding geometry and patch size if the gold etching time was increased. An

x-bonding geometry was obtained from a time range of 0 seconds to 100 seconds, and a Y-bonding geometry was observed after 100 seconds.<sup>8</sup> The polar angle associated with patch size as a function of etch time is shown in Figure 2.4-b, and an illustration of patchy particle formation using Chen's techniques is shown in Figure 2.4-a.

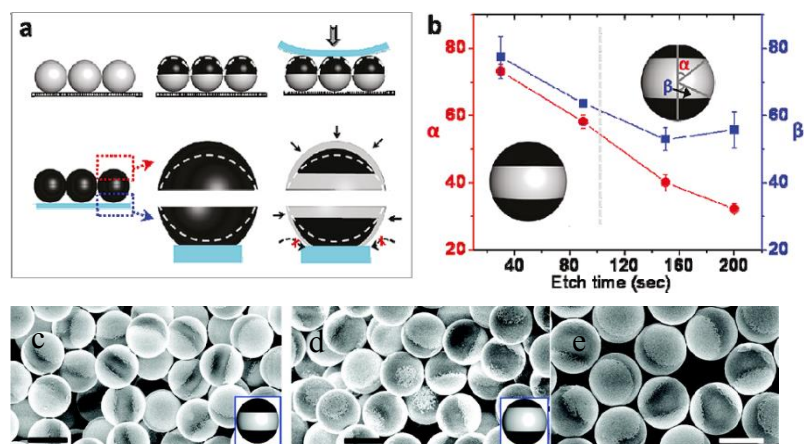


Figure 2.4: (a) Schematic of patchy particle preparation from colloidal monolayer: [1] metal deposition up to hemisphere, particle stamping, repeat [1], etching preferential from equatorial plane. (b) Change in polar angle (associated with patch size) as a function of etch time. Asymmetric patches form at times greater than 100 s. (c-e). Scanning electron microscope images of patchy particles with X, Y, and Z-bonding geometries.[8]

### 2.1.2 Janus particles

Janus-type particles are particles with two different “faces”.<sup>9-11</sup> In other words, a Janus particle has both polar and apolar faces. Figure 2.5-a shows an illustration of a Janus particle. The patch size of the Janus particle can change by varying the half opening angle,  $\theta_{ap}$ . In Figure 2.5-b, an SEM shows a three-dimensional illustration of the silica Janus particles containing gold patches fabricated using thin film evaporation. The

hemispheres with brighter regions contain gold material, and the gray hemispheres are silica material.<sup>10-11</sup>

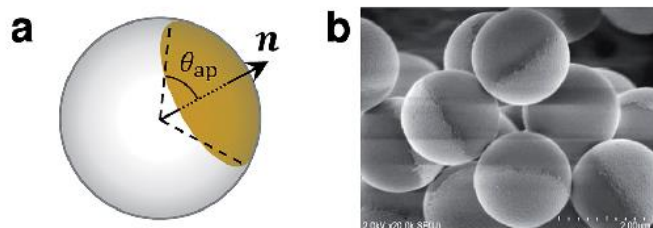


Figure 2.5: (left) Illustration and scanning electron microscope image of one-patch Janus particle. (right) Schematic models and optical images of Janus particles confined in a wedge cell.[11]

Janus particles are potential application materials that can be used in biological sensors, antireflection coatings, and optical devices.<sup>12</sup> Iwashita and Kimura carried out experiments and computational Monte Carlo simulations on Janus particles. Janus particles were dispersed in a binary mixture of 2,6-lutidine and pure water and confined in a wedge-cell. The particles were characterized using an optical microscope that illustrated particle patterns. The wedge-cell was prepared using two cover glass slips where one cover glass was treated at high temperatures (500 Celsius) to make it hydrophilic, while the second cover glass was chemically modified using perfluorodecyltriethoxysilane to make it hydrophobic.<sup>11</sup> Figure 2.6-a through Figure 2.6-d show optical images of Janus particles confined in a wedge-cell. Figure 2.6-e show schematic models of the Janus particles confined in solution, and the pattern formation process is shown on the optical images in Figure 2.6-a through Figure 2.6-d.

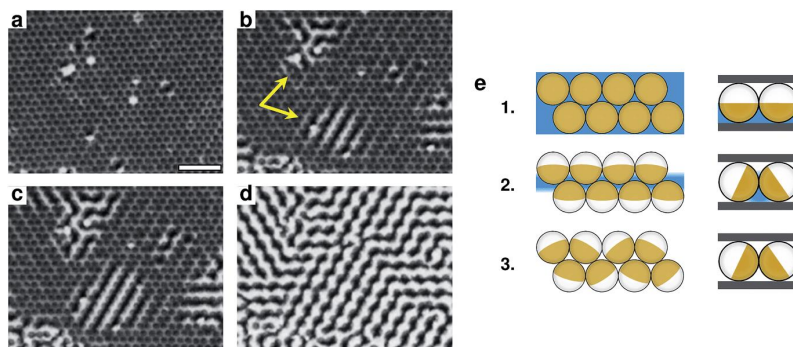


Figure 2.6: Optical images of Janus particles in binary mixture confined in wedge-cell and models of the particle patterns in wedge cells.[11]

The schematic model (1) in Figure 2.6-e corresponds to Figure 2.6-a, and the schematic model (2) corresponds to Figure 2.6-b and Figure 2.6-c. Drawing 3 in Figure 2.6-e is represented in Figure 2.6-d. Drawing 1 corresponds to (a), drawing 2 to (b) and (c), and drawing 3 to (d).<sup>11</sup> The wedge-cell was heated at temperatures above the critical temperature of the solvent, which led to a change in particle pattern from a short-range zigzag stripe pattern into a homogeneous hexagonal array shown in Figure 2.6-a. Cooling the confined Janus particles to lower temperatures than the critical temperature resulted in a change in pattern to a zigzag stripe pattern with monodomains, defects, or grain boundaries as shown in Figure 2.6-b and Figure 2.6-c. A more ordered zig-zag stripe pattern was obtained by heating the sample at temperatures closer to the critical temperature of the solvent. Iwashita and Kimura showed a method that can produce particle patterns in a confined space and showed the effect of solvent phase transitions on particle ordering by exposing confined Janus particles in solution at various different temperatures.<sup>11</sup>

### 2.1.3 Confinement of Anisotropic Colloids

Confinement studies on colloidal particles have shown unique pattern formations. In Muangnapoh's work, silica hollow peanut particles were confined in a wedge-cell and visualized using a confocal laser scanning microscope.<sup>13</sup> The depth profiles of the wedge-cell containing silica hollow peanut particles are shown in Figure 2.7.

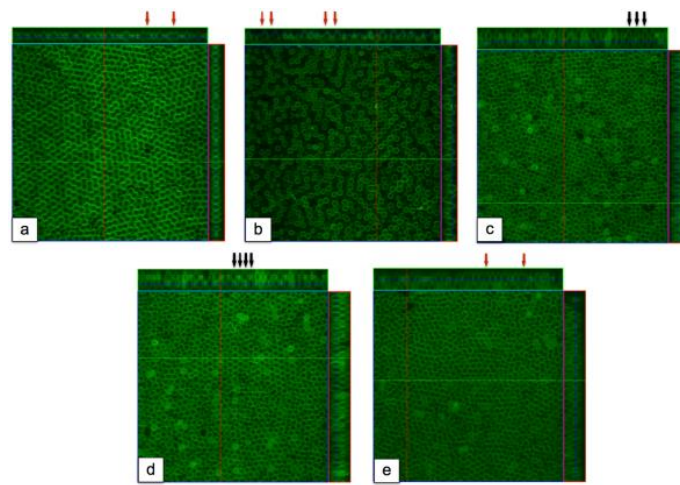


Figure 2.7: Confocal microscopy images (z-slice, side views) for anisotropic colloids (not patchy) under confinement. (a) aligned in-plane, hexagonal monolayer ( $1\Delta$ ) (b) buckled state ( $1B$ ) (c) bilayer square structure ( $2\Box$ ) (d) bilayer hexagonal type I ( $2\Delta_I$ ) (e) bilayer hexagonal type II ( $2\Delta_{II}$ ).[13]

The confocal laser scanning microscopy images reveal different patterns and arrangements of colloidal silica hollow nonspherical particles. The arrangement of particles in Figure 2.7-a shows an hexagonal monolayer, and in the next image (Figure 2.7-b), the particles are arranged in a buckled state. A bilayer square structure, a bilayer hexagonal type I, and a bilayer hexagonal type II are obtained as well as observed in Figure 2.7-c through Figure 2.7-e. The variation of ordering and particle patterns is due to the gap height of the wedge cell. The positions and arrangement of

the particles in the wedge cell vary as gap height is increased. The development of hexagonal and square symmetric arrangements determined as a function of gap height is represented as  $1\Delta \rightarrow 2\Box \rightarrow 2\Delta \rightarrow 3\Box \rightarrow \dots \rightarrow n\Delta \rightarrow (n+1)\Box \rightarrow (n+1)\Delta$ , where  $n$  is the number of layers in the colloidal thin film. Monte Carlo simulations confirmed the experimental results shown in Figure 2.7 above where silica peanut particles were represented as dimers and the arrangements of the dimers in confined walls yielded different phase structures as gap height was varied. The phase structures are modeled in Figure 2.8-a through Figure 2.8-f.<sup>13</sup>

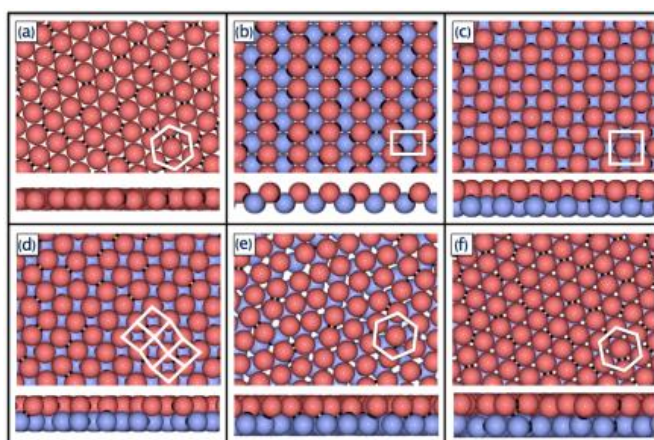


Figure 2.8: Monte Carlo simulations for phase behavior corresponding to experiment. Rhombic phase (d) not observed due to challenging in reaching highest density phase regions.[13]

Monte Carlo simulations can provide information on gap height,  $H$ , as a function of packing fraction,  $\phi$ , and from this computational data, the fraction of particles oriented out-of-plane can be calculated. The color map in Figure 2.9 shows the symmetric arrangements obtained from experiments and simulations and the gap height ranges that correspond to each phase structure.<sup>13</sup>

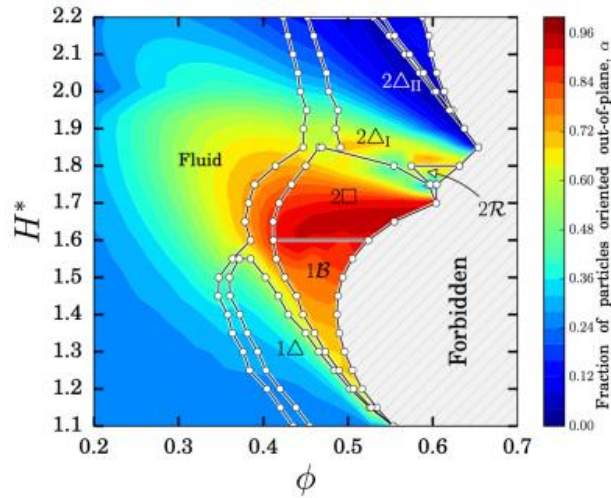
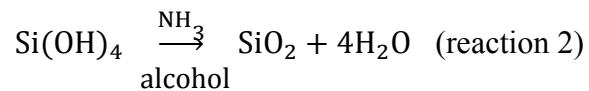
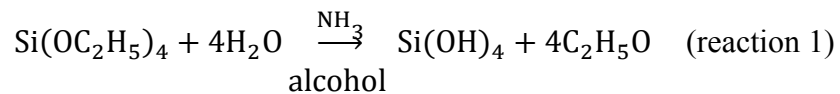


Figure 2.9:  $H^*$ - $\phi$  phase diagram of dimers.[13]

#### 2.1.4 Stöber Method

The hydrolysis of the alkoxysilane used in this study with water is shown in the first reaction shown below. The alkoxysilane reacting with water is tetraethylorthosilicate. The hydrolysis of tetraethylorthosilicate is base-catalyzed by ammonia. The ammonia will negatively charge the surface of the silica particles. The condensation of  $\text{Si}(\text{OH})_4$  is shown in reaction 2 and base-catalyzed with ammonia. The product of the hydrolysis and condensation of tetraethylorthosilicate is silica ( $\text{SiO}_2$ ). The base-catalysis is accompanied with ethanol, an alcohol that can assist in obtaining uniform silica particles.<sup>14-20</sup>



The final particle size is influenced by the ionic strength of the reaction medium, such as the concentration of ammonia and water, and the rate of hydrolysis reaction is influenced by the strength and concentration of the acid or base catalyst. The reaction temperature and the solvents used in the reaction (i.e., ethanol) have secondary effects on the particle size.<sup>15</sup>

## 2.2 Experimental Methods

### 2.2.1 Synthesis of fluorescent silica particles

Fluorescent silica monodisperse microparticles were synthesized and prepared to microfabricate patchy colloidal particles needed for confinement studies of microparticles in wedge-cells. The Stöber method was applied to make silica monodisperse particles where tetraethylorthosilicates, ammonium hydroxide, ethanol, and water were used to make 600 nm monodisperse silica particles. Rhodamine B isothiocyanate is mixed thoroughly to a mixture of 98% tetraethylorthosilicate (Sigma-Aldrich), 25% ammonium hydroxide (Sigma-Aldrich), absolute ethanol (EMSURE), and 18 millipore (mΩ) water.<sup>16</sup> The concentrations of each particular component in the mixture are shown in Table 2.1.

Table 2.1: Concentrations of chemicals used in the synthesis of 600 nm silica particles.

Component	Molarity (M)
Water	2.8
Ammonia	0.72
Ethanol	15.1
TES, 98%	0.17

Monodisperse silica particles were stabilized first by stirring 670 mL absolute ethanol, 51 mL 25% ammonium hydroxide, and 28 mL of 98% tetraethylorthosilicate. It was determined from previous trials of silica synthesis that RITC made the silica particles aggregate in the solution if added during the core growth. Rhodamine B isothiocyanate was added after making 400 nm silica core particles. Pure water and tetraethylorthosilicate were added in intervals every two hours to synthesize core-shell silica particles. After having 400 nm diameter size core-shell silica particles, RITC was added and subsequently more 98% tetraethylorthosilicate and milli-Q water was added in intervals until a diameter size of 600 nm was reached. Table 2.2 provides information on the quantities and volume used for each component used in the synthesis of fluorescent silica monodisperse particles with a final diameter size of 600 nm.<sup>14</sup>

Table 2.2: TES and milli-Q water volume and molar information for silica synthesis.

	200 nm to 400 nm				400 nm to 600 nm			
Interval: 2 h Volume TES & DI Water	1st interval Volume (mL)	2nd interval Volume (mL)	3rd interval Volume (mL)	4th interval Volume (mL)	5th interval Volume (mL)	6th interval Volume (mL)	7th interval Volume (mL)	8th interval Volume (mL)
TES	63.000	63.000	63.000	64.000	63.000	63.000	63.000	64.000
Total DI Water in Vessel	97.244	163.835	230.426	298.073	363.927	430.589	497.106	564.754
DI Water Added	58.994	66.591	66.591	67.648	65.854	66.662	66.517	67.648
Interval: 2 h Volume TES & DI Water	1st interval moles	2nd interval moles	3rd interval moles	4th interval moles	5th interval moles	6th interval moles	7th interval moles	8th interval moles
TES	0.415	0.699	0.984	1.272	1.554	1.838	2.122	2.411
DI Water	5.396	9.092	12.787	16.541	20.196	23.895	27.586	31.340

## 2.2.2 Preparation of colloidal solutions & silicon substrates

In addition to fluorescent silica monodisperse particles, dimers and hollow peanut-shaped particles were microfabricated as well. The PMMA dimers and hollow peanut-shaped particles were synthesized by Lyons, K. and Muangnapoh, K. in the Liddell-Watson lab. The particles were also used to eventually obtain patchy non-spherical particles for confinement studies of gold-coated particles. The solvents used for making particle solutions used in spin-coating were 200-proof ethanol (Koptec) and n-

butanol (Aesar). Silica microparticles with a size of 400 nm were centrifuged at speeds in the range of 700 rpm and 1000 rpm to remove ethanol and ammonia mixtures for ten minutes. Ethanol was added to the pellet of silica particles, and the resuspension of particles was accomplished using an ultrasonicator. The fluorescent 400 nm silica microparticles were sonicated in ethanol for more than ten minutes. Tumbling was another technique used to make particles stable in solutions by adding a 50 mM polyvinylpyrrolidone (PVP) in water solution onto silica hollow peanut particles. The silica hollow peanut particles in PVP-H<sub>2</sub>O mixture were tumbled for twenty-four hours in a rotating machine that mixed the particles in PVP and water solution. The PVP and water solution was removed by centrifuging the particles in water and ethanol a couple of times at speeds of 1000 rpm for five minutes. The silica hollow peanut particles were resuspended in n-butanol or ethanol for making monolayers of particles on substrates. PMMA dimer particles were sonicated in ethanol for about ten minutes and longer to make sure the particles were suspended well. Many colloidal particle suspensions were prepared for the study of patchy particles. Table 2.3 shows the concentrations of particles in solvents and the centrifugation speeds used to remove solvents for making clean colloidal suspensions.

Table 2.3: Parameters and Conditions used to make colloidal suspensions.

Particle Type	Solvent	Concentration (g/mL)	Centrifugation Speed (rpm)	Centrifugation Time (min)
400 nm fluorescent silica microspheres	Ethanol	0.11	500, 550	1 min, 1 min
PMMA dimers	Ethanol	0.028	3000, 2500, 2000	35 min, 25 min, 25 min
Silica hollow peanut particles	n-butanol	~0.02	1000, 1500	10 min, 10 min
2 um silica microspheres	n-butanol	0.04	8500	7 min

All silicon wafers and silicon substrates were cleaned using a piranha etching solution which consisted of 70% sulfuric acid (BDH) and 30% hydrogen peroxide (Fisher Scientific). Silicon substrates were placed in a 3:1 hydrogen peroxide and sulfuric acid solution for thirty minutes. Deionized water was used to rinse silicon substrates after piranha etching the substrates. The silicon substrates were dried with dry nitrogen and stored in wafer cassettes until further use.

### **2.2.3 Spin-coating**

In order to make gold-coated particles, the particles needed to be spin-coated prior to thin film evaporation. Colloidal particle suspensions were sonicated for a minute and immediately deposited on the center of the silicon substrates prior to spin-coating. Spin-coating was applied to all particles to obtain a monolayer of particles on silicon wafer substrates. A spin coater model P6700 series was used with three spin-coating steps. The spin-coating conditions applied to silica particles and non-spherical particles varied from 200 rpm to 4000 rpm. The substrates were allowed to dry over a period of two to three hours for imaging due to excess solvent remaining after spin-coating which needed a period of evaporation.

### **2.2.4 Thin film deposition**

Silicon wafers with monolayers of particles were placed on an electron-beam evaporator to deposit 25 nm gold (Au) and 2 nm titanium (Ti) onto the hemispheres of particles. Janus-type particles only require one deposition of gold and titanium on one side of the particle, whereas patchy particles require deposition of gold and titanium thin films on both hemispheres of particles. The amount of titanium deposited was

varied from 2 nm to 10 nm for better adhesion of gold onto particles. Titanium was deposited first, and gold was deposited later. A vacuum pressure of less than  $2 \times 10^{-6}$  Torr was reached during electron-beam evaporation to deposit a smooth thin film of titanium and gold.

### **2.2.5 Lift-off Techniques**

Elastomeric stamps were prepared earlier to lift off monolayers of particles after thin film deposition. Polydimethylsiloxane (PDMS) stamps were made by preparing a 10:1 weight ratio of Sylgard 184 elastomer and curing agent mixture. The Sylgard 184 elastomer and curing agent mixture was placed under vacuum to remove any bubbles in the mixture and transferred to petri-dishes at room temperature. The PDMS was cured at room temperature for a period of twenty-four hours. Plasma treatment was performed on PDMS stamps using a Harrick plasma cleaner. The PDMS stamps were treated with plasma for a period of 90 seconds. Plasma-treated PDMS stamps were used to lift one-sided gold coated particles off silicon substrates by applying hand-pressure onto PDMS stamps that were placed above gold coated silicon substrates containing colloidal particles. The PDMS stamps were typically removed after applying pressure for sixty seconds. Thin film evaporation was repeated onto PDMS stamps containing gold particles that were embedded on the surface of PDMS.

### **2.2.6 Gold etching**

PDMS stamps containing gold coated particles were transferred onto gold etching solutions to etch gold from the particles in order to obtain triblock patchy particles. Gold etching solutions were prepared by preparing a solution containing 0.156 M

sodium thiosulfate, 1.026 mM potassium ferrocyanide, 10.13 mM potassium ferricyanide, 0.998 M potassium hydroxide in 17 milliohms deionized water. The PDMS stamps were removed from gold etching solutions after reaching a desired and specific triblock geometry (x-bonding, y-bonding, k-bonding) usually within a period of 30 seconds to 120 seconds. Immediately, the PDMS stamps were immersed into milliQ water to remove any excess gold etching liquid off the PDMS stamps to prevent further gold etching.

### **2.2.7 Thiol treatment**

The gold etched PDMS stamps were treated with an alkanethiol to modify the surface chemistry of gold particles with a thiol hydrocarbon ligand to make hydrophobic patchy colloidal particles. A solution containing 2 mM octadecanethiol in ethanol was prepared and deposited onto gold-etched PDMS stamps for a time period of 2 hours. Afterward, ultrasonication was applied onto PDMS stamps to remove gold patchy particles by placing the PDMS stamps on petri-dishes or glass vials to store patchy particles for imaging.

### **2.2.8 Characterization**

A scanning electron microscope (SEM) was used to image monolayers of colloidal particles on silicon substrates and also characterize patchy particles. Fluorescent silica monodisperse particles were also characterized using an SEM. The typical voltages used for colloidal particles and patchy particles were in the range of 1 kV to 5 kV. Samples were carefully dried prior to SEM imaging using dry nitrogen or applying

gold palladium onto the samples in a sputtering system. The average diameter of microspheres was calculated using equation 1.

$$\bar{x} = \frac{1}{N} \sum_{i=1}^N D_i \quad (1)$$

The standard deviation was calculated using equation 2.

$$\sigma = \sqrt{\frac{1}{N-1} (x_i - \bar{x})^2} \quad (2)$$

The coefficient of variance was determined using the average diameter and the standard deviation and calculated using equation 3. The coefficient of variance provides the polydispersity of particles after synthesis.<sup>14</sup>

$$CV = \frac{\sigma}{\bar{x}} \quad (3)$$

### 2.2.9 Confinement

The confinement of patchy particles and Janus particles will occur in wedge-cells. The wedge-cells can be prepared using 3 inches by 2 inches glass slides and two 50 mm by 22 mm coverslips as shown in Figure 2.10. For sealing the wedge-cells, UV glue will be used, and hand pressure can be applied to seal the cover slips onto the glass slides. The sides of the wedge-cell are sealed to eliminate the evaporation of the solvent in the wedge-cell.

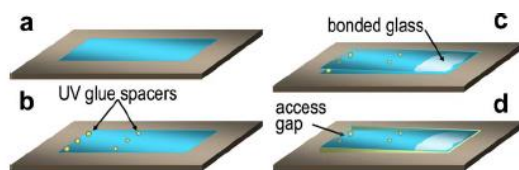


Figure 2.10: Illustration of wedge-cells containing glass slides and cover slips.[22]

Multilayers of patchy colloidal particles will be obtained by highly concentrating the wedge-cell with a solution of patchy particles, and the lowest gap height will be visualized using an optical fluorescence microscope and a confocal laser scanning microscope, which can extract profiles of the sample at various depths (z-axis). The gap height can be illustrated in Figure 2.11, which is the space that separates the cover slip labeled A and the glass side labeled C.

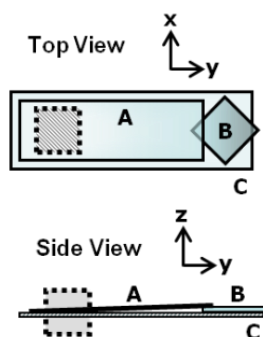


Figure 2.11: Top view and side view of a wedge-cell.[13]

In this study, the challenge will be visualizing particle layers below the top layer since the light from laser equipment will not penetrate gold material and metals, and the light will be scattered. Therefore, we will aim to only image the top layers of the wedge-cell and observe if any structures or patterns formed after patchy particles are confined in solution.<sup>21</sup> The wedge-cell will be used to control the self-assembly of

patchy particles into well-defined crystal structures that can have different phases and lattices with gap height.

## 2.3 Results

### 2.3.1 Fluorescent Silica Monodisperse Particles

Fluorescent monodisperse silica particles were obtained with a final diameter size of approximately 600 nm as shown in Figure 2.12.

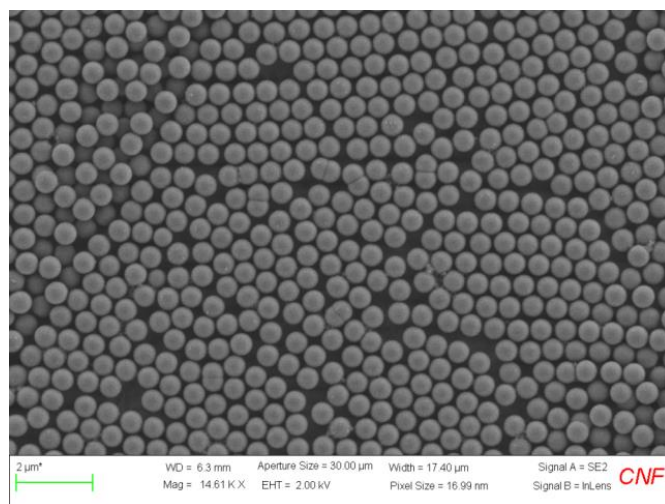


Figure 2.12: Fluorescent (RITC) silica particles synthesized using Stöber method with an average diameter of 580 nm and a coefficient of variation of 4.8%. Image illustrating crystallization and hexagonal packing of silica ( $\text{SiO}_2$ ) particles.

The average diameter size is 580 nm with a coefficient of variation of 4.8%, which was calculated using ImageJ software and an SEM image shown in Figure 2.13 that contained a single monolayer of particles for accurate average calculations. Figure 2.13 shows a characteristic of colloidal crystallization on the right region of the image with various particles forming an hexagonal close-packed arrangement.

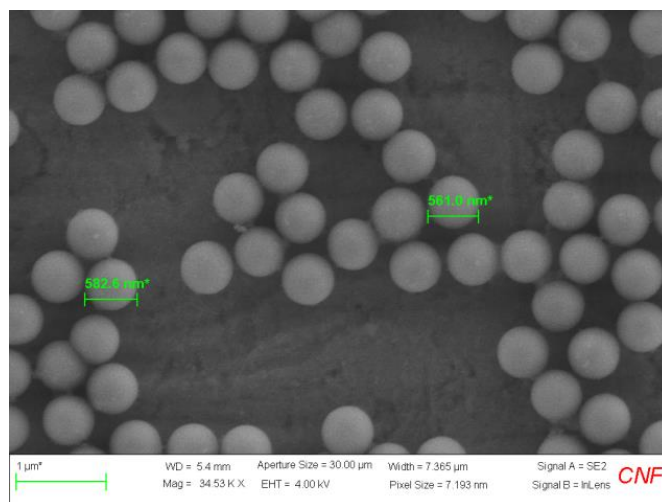


Figure 2.13: Higher magnification of monodisperse fluorescent (RITC) silica particles synthesized using Stöber method with an average diameter of 580 nm and a coefficient of variation of 4.8%.

### 2.3.2 PMMA Dimers

PMMA dimers were used to make patchy nonspherical particles to determine if titanium can strongly attach to the surface of PMMA nonspherical particles. The PMMA dimers used in the microfabrication experiments are shown in Figure 2.14 below.

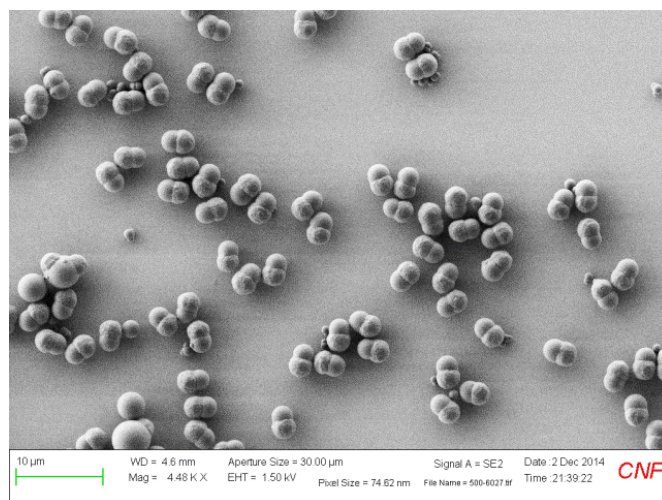


Figure 2.14: Poly(methyl methacrylate) [PMMA] dimers spin coated at 500 rpm for 60 s in ethanol.  $[PMMA]_{Si<100>} = 0.02795 \text{ g/mL}$ .

### 2.3.3 Hollow Silica Peanut Particles

The hollow silica peanut-shaped particles were also used to determine if the hollow particles can sustain the hand pressure applied during PDMS stamping. The hematite peanut-shaped core particles without a silica outer shell are shown in Figure 2.15. The hollow silica particles are synthesized using a hematite core, and the core is removed using hydrochloric acid, which removes hematite and does not remove the silica outer shell. The thickness of the silica outer shell is approximately 100 nm.

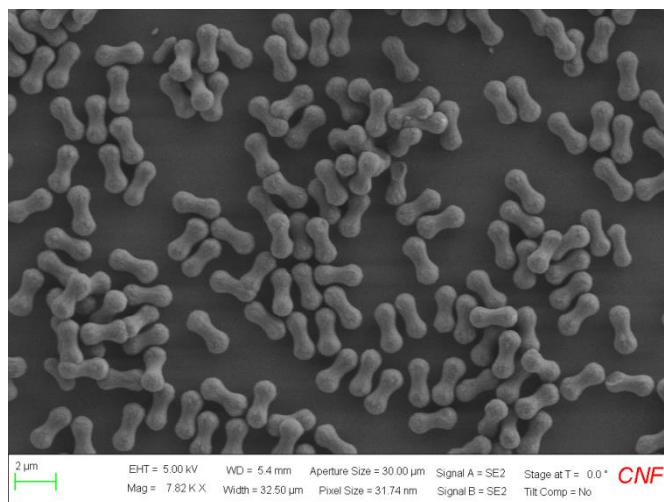


Figure 2.15: Poly(methyl methacrylate) [PMMA] dimers spin coated at 500 rpm for 60 s in ethanol.  $[\text{PMMA}]_{\text{Si}<100>} = 0.02795 \text{ g/mL}$ .

### 2.3.4 Spin-coating silica particles

Spin-coating parameters were determined for smaller diameter size silica monodisperse particles to obtain a range of speeds and time frames at which fluorescent silica particles formed a monolayer on a silicon wafer. The objective is to minimize aggregates and clumps of particles on a silicon wafer in order to have

uniformly coated particles after thin film deposition. A 3-in wafer was used as shown in Figure 2.16 and Figure 2.17 to have a higher surface coverage area of particles and obtain a high concentration of patchy particles and Janus-type particles for confinement studies. The 400 nm fluorescent silica colloidal particle solution was spin-coated on a 3-in silicon wafer at 500 rpm and 550 rpm for 60 seconds each step. The concentration of silica particles on the 3-in silicon wafer is 0.111 g/mL. The difference between Figure 2.16 and Figure 2.17 is the brilliance characteristic that appears at a tilt angle. In both figures, the same wafer was used to illustrate the change in color as the wafer was tilted. In Figure 2.16, the wafer is lying flat on a petri-dish, but it shows less brilliance compared to Figure 2.17 where the wafer is tilted at an angle, demonstrating an opalescence characteristic of crystallization in colloidal close-packed particles.

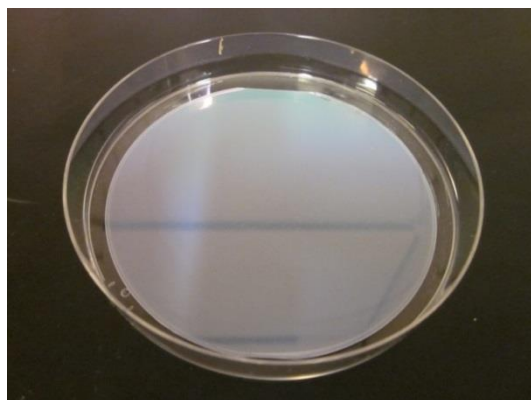


Figure 2.16: Photograph of a 3-in silicon wafer containing a monolayer of 400 nm fluorescent silica particles.  $[\text{SiO}_2]_{\text{Si}<100>} = 0.111 \text{ g/mL}$ .



Figure 2.17: Photograph of a 3-in silicon wafer showing brilliant opalescence of a monolayer of 400 nm fluorescent silica particles.

### 2.3.5 Spin-coating nonspherical particles

PMMA dimers in ethanol were spin coated at 500 rpm for 60 seconds, and the concentration of the particles in the 4-in silicon wafer was 27.95 mg/mL. A lower concentration was achieved in PMMA dimers compared to silica particles because a larger wafer was used. The diameter size of the substrate can range from 3-in to 4-in, but the amount of particles in solvent needs to be increased as the size of the substrate is increased. A higher concentration of PMMA dimers is needed to make a close-packing arrangement of PMMA dimers and minimize the gaps between particles to prevent gold excess after removal of gold-coated particles. The silica hollow peanut particles were spin-coated at a speed of 200 rpm and 300 rpm for 30 seconds at each step. The concentration of the silica hollow peanut-shaped particles on the 4-in silicon wafer after spin coating was 0.0365 g/mL. The surface coverage of hollow peanut particles are shown in Figure 2.18, which shows a non-close packed arrangement of particles.

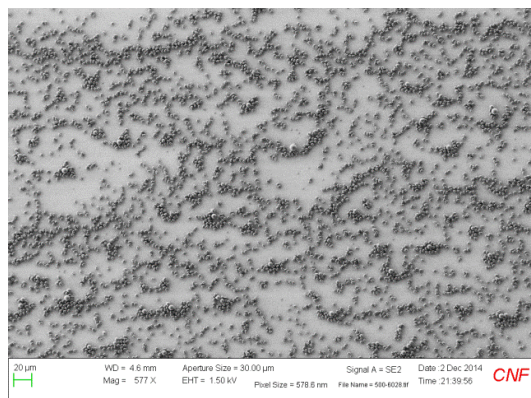


Figure 2.18: Surface coverage of PMMA dimers spin coated at 500 rpm for 60 s in ethanol.

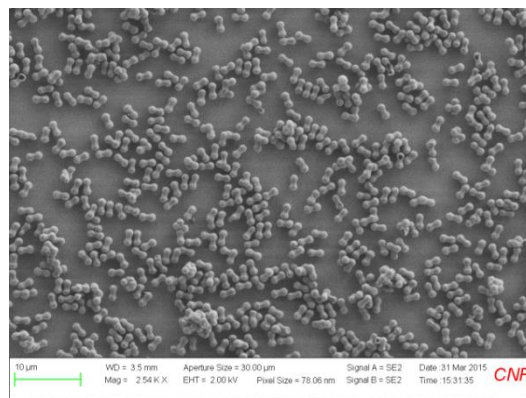


Figure 2.19: SiO<sub>2</sub> hollow peanut-shaped particles spin coated at 200 rpm and 300 rpm for 30 s in ethanol  
 $[H]_{Si<100>} = 0.0365$  g/mL.

A close-packing arrangement of silica hollow peanut-shaped particles is challenging to achieve using the spin-coating method due to the centrifugal forces causing particles to lay above each other. Aggregates and clumps were observed after spin coating silica hollow peanut-shaped particles which can be minimized by sonicating particles for a longer time and using more PVP to stabilize particles. Fluorescent silica particles with a diameter size of 400 nm were spin coated at 500 rpm and 550 rpm for 60 seconds at each step on a 3-in silicon wafer. Figure 2.20 shows a higher surface coverage of particles on a substrate with less open gaps. In Figure 2.20, we observe several clumps and coalescent particles after spin coating. The coalescent particles are present before spin coating due to aggregation and instability during the synthesis of silica particles as a result of rhodamine B isothiocyanate effects on core silica particles. The synthesis of fluorescent silica particles was controlled further by inserting RITC after making 400 nm silica core particles. Experiments on 400 nm fluorescent silica particles provide spin-coating conditions that can be used for larger particles (600 nm). Spin-coating speeds in the range of 500 rpm and 650 rpm can be used on 600 nm fluorescent silica particle solutions to yield a monolayer and a close-packed arrangement of particles in a 3-in silicon wafer.

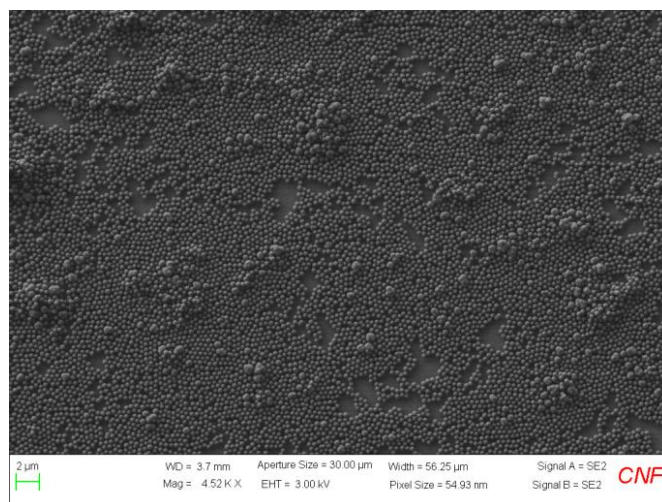


Figure 2.20: SEM image of 400 nm fluorescent silica particles spin coated at 500 rpm and 550 rpm for 60 s on a 3-in silicon wafer.

### 2.3.6 Nonspherical Patchy Particles

Figure 2.21 illustrates an SEM image of PMMA nonspherical particles with gold coated hemispheres and a titanium and PMMA middle band. Thin film deposition and PDMS stamping were achieved on PMMA dimers as shown in Figure 2.21. In the figure, we observe smaller dimers coming from synthesis solutions which can be removed using improved centrifugation steps and synthesis techniques. A thin film of gold (25 nm) and 4 nm titanium were deposited onto PMMA dimers. The gold coating in the PMMA dimers was etched for 60 seconds.

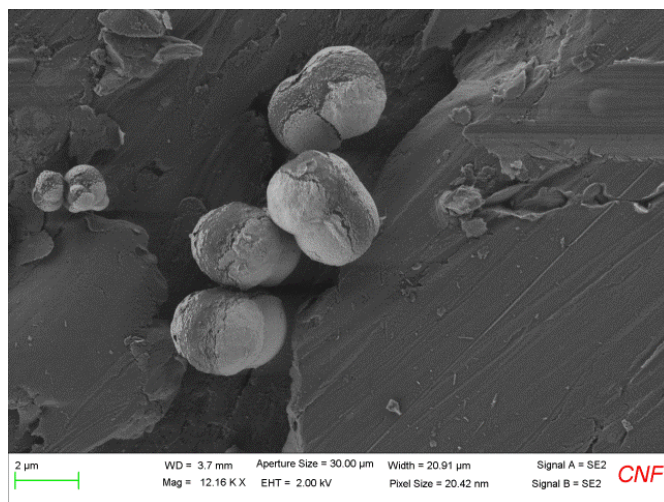


Figure 2.21: PMMA patchy particles with X-bonding geometry having 25 nm Au and 4 nm Ti coating and a gold etching time of 60 s.

Figure 2.22 shows a different region of the sample that was imaged using an SEM in Figure 2.21. In Figure 2.22, we note a difference in the background and materials that are not PMMA dimers. Excess gold thin films were present in the sample after sonication of the PDMS stamps. The excess gold and titanium thin films are present due to open gaps in the wafer substrates which were coated. The excess gold thin films can be reduced by sonicating for a shorter time and also by increasing the coverage of

particles on silicon substrates. In confinement studies and self-assembly of nonspherical PMMA particles in wedge-cells, it is essential to have a clean sample of particles.

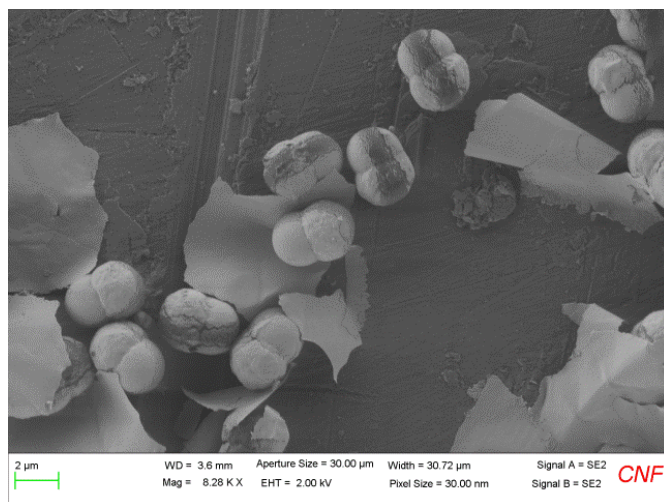


Figure 2.22: PMMA patchy particles with X-bonding geometry having 25 nm Au and 4 nm Ti coating and a gold etching time of 60 s and excess gold thin films.

Silica hollow peanut-shaped patchy particles are shown in Figure 2.23. The amount of titanium deposited onto the particles was 3 nm. Based on the SEM image below, the shape of the hollow particles remained intact after PDMS stamping and thin film deposition as well as sonication. Additionally, we noted many excess gold thin films in the SEM stub, which is a result of low surface coverage of hollow silica peanut-shaped particles on silicon substrates.

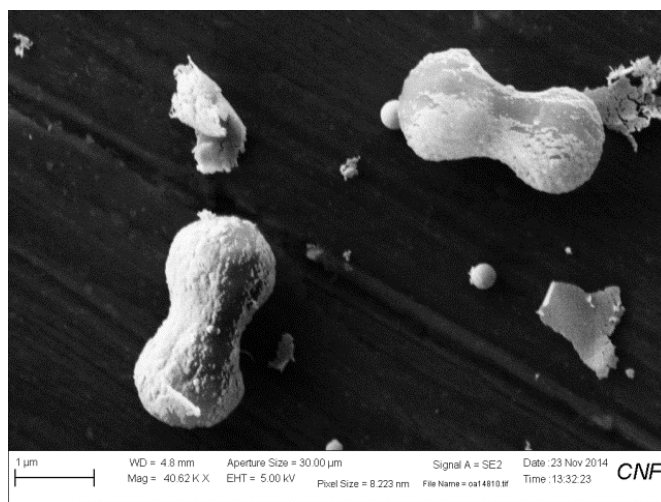


Figure 2.23: SiO<sub>2</sub> hollow peanut-shaped patchy particles (X-bonding) having 25 nm Au and 3 nm Ti coating and a gold etching time of 90 s.

### 2.3.7. Confinement Silica Patchy Particles

Small-scale experiments on silica monodisperse spherical particles were first performed to obtain patchy silica microparticles for confinement studies in a wedge-cell. From these experiments (Figure 2.24-d, 2.24-c), we determined that it was necessary to have a concentrated patchy particle solution after thiol treatment. In Figure 2.24-a, we show the monolayer of 2 μm commercialized silica particles (Bangs Laboratories) obtained using a spin-coating speed of 4000 rpm for 60 seconds. The patchy silica microparticles are shown in Figure 2.24-d where it is observed that the particles have gold patches with some particles missing patches. Uniformity in particles is essential and can be achieved by initially having a monolayer of silica particles with few aggregates and clumps. The patchy particles in Figure 2.24-d were gold etched for 100 seconds and the tilt angle of metal deposition was normal to the

plane of the substrates, which yielded particles that can form an X-bonding geometry when assembled in solution.

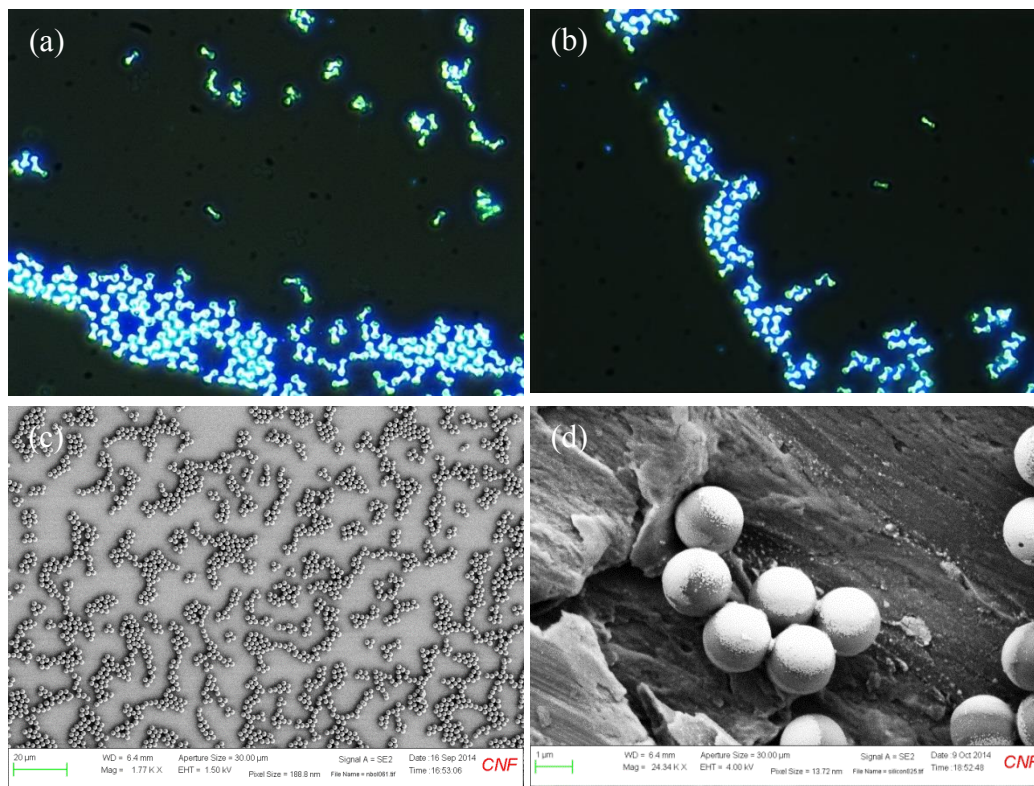


Figure 2.24: (a) Optical image of fluorescent 2  $\mu\text{m}$  silica patchy particles confined in a wedge cell. Image taken by Angela Stelson. (b) second optical image of fluorescent 2  $\mu\text{m}$  silica patchy particles confined in a wedge cell. Image taken by Angela Stelson. (c) 2  $\mu\text{m}$   $\text{SiO}_2$  microparticles (4% solids) spin-coated at 4000 rpm for 60 s in n-butanol. (d) 2  $\mu\text{m}$   $\text{SiO}_2$  patchy particles (X-bonding) with 25 nm Au : 2 nm Ti coating & etched for 100 s.

Patchy 2  $\mu\text{m}$  silica microparticles were confined in a wedge-cell and observed under a fluorescent microscope to note any crystal structure formation. It is observed in Figure 2.25-a and 2.25-b that there is a low quantity of patchy particles, but we can observe particles arranging next to each other at the lowest gap height.

The patch size of silica microsphere particles was varied in small-scale experiments by varying the gold etching time that silica gold coated particles were exposed after thin

film deposition and PDMS stamping. We achieved larger gold patches with a gold etching time of 40 seconds in X-bonding type silica patchy particles as shown in Figure 2.25-b. Larger patches are achieved by reducing the gold etching time. In Figure 2.25-b, we observed smaller patches due to exposing silica gold-coated particles for 100 seconds.

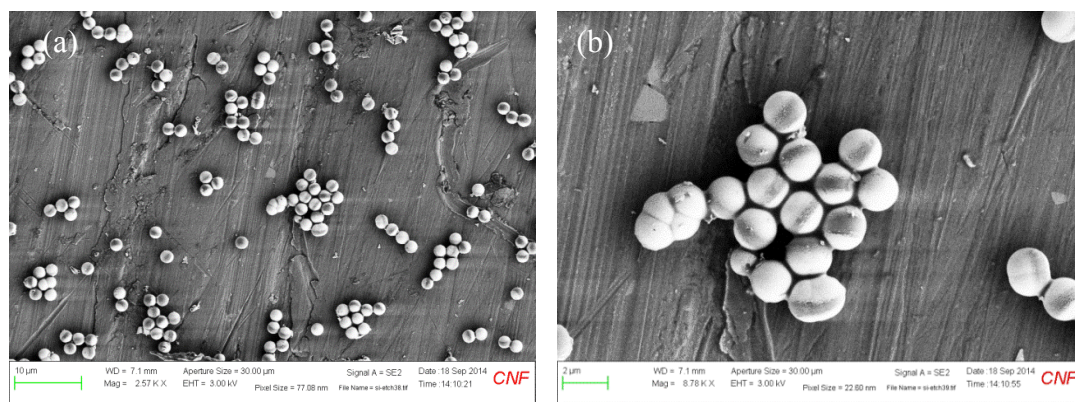


Figure 2.25: (a) 2  $\mu\text{m}$  silica patchy particles (X-bonding) with 25 nm Au and 2 nm Ti coating and gold etched for 40 s (b) selected particles in (a).

## 2.4 Research Plan

### 2.4.1 Confinement of Janus particles

After the microfabrication of 600 nm fluorescent silica Janus particles, the next step will be to confine the particles in a wedge cell to find any particular structures after confinement. Confocal laser scanning microscopy will be used to visualize the top layer of confined fluorescent Janus particles. In these confinement studies, different solvent media will also be used to note any particular effects of solvent media on particle arrangements. Additionally, the temperature of the solvent and Janus particles will be modified from room temperature to lower temperatures and higher temperatures to observe any thermal effects on particle ordering. Different organic

ligands, such as smaller alkanethiols (i.e., hexanethiol), will be applied onto Janus silica particles to observe any effect of alkyl chains on particle ordering. Electric fields will later be introduced onto the Janus particles confined in a wedge-cell to note any crystal structure deformation.

#### **2.4.2 Confinement of Nonspherical Janus Particles**

The aim of microfabricating and confining spherical Janus particles is to eventually microfabricate and confine Janus nonspherical particles. PMMA Janus dimers and silica peanut-shaped Janus particles will be confined separately in wedge-cells. Particle order and arrangements will be visualized using confocal laser scanning microscopy. Similar studies applied to Janus silica particles discussed in section 2.4.1 will be applied to nonspherical Janus particles. We have decided to only confine Janus spherical and nonspherical particles since patchy particles resulted in more excess gold thin films in solution. Filtration techniques and repeated centrifugation techniques, however, can be used to remove excess gold and titanium thin films.

#### **2.4.3 Monte Carlo Simulations**

After confining Janus silica spherical particles and nonspherical particles, the next step is to simulate Janus dimers and Janus spheres in wedge-cells to determine phase diagrams discussed in previous sections. Monte Carlo simulations will be applied onto Janus particle models to compare computational data with experimental results. Monte Carlo simulations can also provide information on the packing fraction of Janus particles in wedge-cells. Lastly, Monte Carlo simulations can provide crystal structures and ordering of Janus particle models that may not be visible in confinement

experiments using confocal laser scanning microscopy as a result of light scattering by metal-coated particles.

## **2.5 Conclusion**

In these studies, we determined that it was necessary to have a higher surface coverage on 4-in and 3-in silicon wafers in all types of particles, both spherical and nonspherical colloidal particles in order to have a highly concentrated solution needed for confinement studies. The next step is to synthesize 600 nm fluorescent silica particles and determine the spin coating parameters to obtain a monolayer of particles in silicon substrates. Optimal spin coating parameters are necessary to make monolayers of nonspherical and spherical particles needed for microfabrication of patchy particles. Monolayers of particles can be obtained using highly concentrated colloidal suspensions and low spin coating speeds in the range of 500 rpm to 800 rpm. Various types of patchy particles can be microfabricated with different geometries by using different glancing angle depositions, varying the gold etching time, and also varying the metal type used during thin film evaporation in order to determine crystal structures and arrangements of these patchy particles in wedge-cells. From our studies, we gained insight on the challenges of microfabricating patchy particles using the lift-off technique where we observed gold excess material in most cases, but we can overcome these challenges by making Janus-type particles in both the nonspherical and spherical colloidal particles. Improvements on colloidal monolayers are needed to have uniform Janus gold coated particles and patchy particles, and this can be achieved by having stable colloidal particles and well-dispersed particles.

## REFERENCES

1. Joannopoulos, J. D. et al., "Photonic Crystals: Molding the Flow of Light", Princeton University Press (2008).
2. Pawar A. B. and Kretzschmar I., "Fabrication, Assembly, and Application of Patchy Particles", *Macromol. Rapid Commun.*, **31**, 150-168 (2010).
3. Velev, O. D., "Curvature makes a difference", *Nature Nanotechnology*, **8**, 620-621 (2013).
4. Du, J. Z. and O'Reilly, R. K., "Anisotropic particles with patchy, multicompartiment and Janus architectures: preparation and application", *Chem. Soc. Rev.*, **40**, 2402-2416 (2011).
5. Rodríguez-Fernández, D. and Liz-Marzán, L. M. "Metallic Janus and Patchy Particles", *Part. Part. Syst. Charact.*, **30**, 46–60 (2013).
6. Jiang, S., Chen, Q., Tripathy, M., Luijten, E., Schweizer, K. S. and Granick, S. "Janus Particle Synthesis and Assembly", *Adv. Mater.*, **22**, 1060–1071 (2010).
7. Yu, C., Zhang, J. and Granick, S., "Selective Janus Particle Assembly at Tipping Points of Thermally-Switched Wetting", *Angew. Chem.*, **126**, 4453–4456 (2014).
8. Chen, Q., Diesel E., Whitmer, J. K., Bae, S. C., Luijten, E., Granick, S., "Triblock Colloids for Directed Self-Assembly", *J. Am. Chem. Soc.*, **133**, 7725-7727 (2011).
9. Chen, Q., Yan, J., Zhang, J., Bae, S. C., and Granick, S., "Janus and multiblock colloidal particles", *Langmuir* **28**, 13555-13561 (2012).
10. Iwashita Y. and Kimura, Y., "Stable cluster phase of Janus particles in two dimensions", *Soft Matter*, **9**, 10694 (2013).
11. Iwashita Y. and Kimura, Y., "Orientational order of one-patch colloidal particles in two dimensions", *Soft Matter*, **10**, 7170 (2014).
12. McConnell, M. D., Kraeutler, M. J., Yang, S., and Composto, R. J., "Patchy and Multiregion Janus Particles with Tunable Optical Properties", *Nano Letters* **10**, 603-609 (2010).

13. Muangnaoh, K., Liddell-Watson, C. M., Avendaño, C., Escobedo, F. A., Degenerate Crystals from Colloidal Dimers Under Confinement. *submitted to Soft Matter*, Aug. 2014.
14. van Blaaderen, A., van Geest, J., and Vrij, A., “Monodisperse colloidal silica spheres from tetraalkoxysilanes: particle formation and growth mechanism”, *Journal of Colloid and Interface Science*, **154**, 2 (1992).
15. Bogush, G. H. and Zukoski, C. F., “Uniform silica particle precipitation: An aggregative growth model”, *Journal of Colloid and Interface Science*, **142**, 1 (1991).
16. Bogush, G. H., Tracy, M. and Zukoski, C. F., “Preparation of monodisperse silica particles: Control of size and mass fraction”, *Journal of Non-Crystalline Solids*, **104** (1988).
17. Vacassy, R., Flatt, R. J., Hofmann, H., Choi, K. S., and Singh, R. K., “Synthesis of Microporous Silica Spheres”, *Journal of Colloid and Interface Science*, **227** (2000).
18. Pontoni, D., Narayanan, T., and Rennie, A. R., “Time-Resolved SAXS Study of Nucleation and Growth of Silica Colloids”, *Langmuir*, **18** (2002).
19. Verhaegh N. A. M. and van Blaaderen A., “Dispersions of rhodamine-labeled silica spheres—Synthesis, characterization, and fluorescence confocal scanning laser microscopy”, *Langmuir*, **10**, 1427-1438 (1994).
20. X. D. Wang, Z. X. Shen, T. Sang, X. B. Cheng, M. F. Li, L. Y. Chen, Z. S. Wang, “Preparation of spherical silica particles by Stober process with high concentration of tetra-ethyl-orthosilicate”, *Journal of Colloid and Interface Science*, **341**, 23–29 (2010).
21. Ruth, D. P. and Gunton, J. D. and Rickman, J. M. and Li, Wei, “The impact of anisotropy and interaction range on the self-assembly of Janus ellipsoids”, *The Journal of Chemical Physics*, **141**, 214903 (2014).
22. Gerbode, S. J., Ong, D., Liddell, C. M., and Cohen, I., “Dislocations and vacancies in two-dimensional mixed crystals of spheres and dimers”, *Phys. Rev. E* **82** 041404 (2010).

## APPENDIX

**Table S1: PbSe and PbS Simulation Cell Dimensions**

Nanocrystal	Slab type	$a_1$ [Å]	$a_2$ [Å]	$k_{b1}$	$k_{b2}$
PbSe	{100}	6.205	6.205	10	10
	{110}	8.775	6.205	7	10
	{111}	8.775	8.775	8	8
PbS	{100}	5.993	5.993	10	10
	{100}	8.476	5.993	7	10
	{100}	8.476	8.476	8	8

**Table S2: Ligand and PbSe and PbS Simulation Cell Dimensions**

Slab Type	Ligand	$N_L$	$a_1$ [Å]	$a_2$ [Å]	$k_{b1}$	$k_{b2}$
{100} PbSe	$N_2H_4$	1	12.41	12.41	7	7
	$C_3H_6S_2$	1	12.41	12.41	7	7
	PbAA <sub>2</sub>	1	18.61	15.47	7	7
	DMF	1,2	12.41	12.41	3	5
	DMF	3,4	18.61	15.47	3	5
{100} PbS	$PbCl_2$	1	11.98	11.98	8	8
{110} PbSe	DMF	1	17.55	12.41	3	5
{111} PbSe	DMF	1	17.55	17.55	4	4

**Table S3: Ligand Simulation Cell Dimensions**

Ligand	$a_1$ [Å]	$a_2$ [Å]	$a_3$ [Å]
DMF	13.0	13.0	13.0
DMSO	15.0	15.0	15.0
$PbCl_2$	15.0	15.0	15.0
$C_3H_6S_2$	10.0	10.0	10.0
PbAA <sub>2</sub>	15.0	12.0	25.0

**Table S4: Permittivity of Polar Solvents at 20°C and Dipole Moments**

<b>Solvent</b>	<b><math>\epsilon</math></b>	<b>Dipole Moment</b>
Hexane	1.89	0.08
Chloroform	4.806	1.15
Ethanol	25.00	1.66*
Dimethylformamide	36.71	3.86
Acetonitrile	37.50	3.44*
Dimethylsulfoxide	46.68	4.1
Propylene Carbonate	64.90	4.94*
Water	80.10	1.87*